Fasihanifard and Packirisamy *Microsystems & Nanoengineering* (2025)11:195
https://doi.org/10.1038/s41378-025-00906-6

Microsystems & Nanoengineering
www.nature.com/micronano

ARTICLE Open Access

Angled electrode comb drives for enhanced actuator in silicon photonic applications

Mohammadreza Fasihanifard[1] and Muthukumaran Packirisamy[1]✉

Abstract

This paper presents an in-depth analysis of electrostatic comb drives, specifically focusing on angled finger configurations to optimize performance for high-demand silicon photonic devices. The study contributes to the advancement of optical microsystems, particularly for beam steering configurations, by simultaneously considering three key figures of merit: traveling range (or displacement), force, and footprint, which are essential for achieving high force intensity and large travel ranges. We investigate critical design parameters such as the number of fingers per arm, their dimensions, and arm dimensions to understand their influence on actuator performance. The research also adheres to design rules for commercially available foundries, ensuring that the proposed designs are manufacturable and suitable for practical implementation. Our findings highlight that angled fingers significantly enhance force intensity and travel range, providing operational flexibility essential for applications requiring a compact footprint alongside high-force capabilities. Through detailed simulations and experimental validations, we demonstrate how specific adjustments in comb drive configuration, like finger geometry and comb arrangement, effectively maintain extensive travel ranges while improving force intensity. We achieved a force intensity of over 200 mN/m^2 through optimized comb configurations and demonstrated how changes in configuration, even with the same finger and arm dimensions, significantly affect the force intensity. Furthermore, we introduce correction functions to compensate for common fabrication discrepancies, such as over-etching, enhancing the precision of manufacturing processes and ensuring alignment with design specifications. This work establishes a robust framework for developing high-performance MEMS actuators that balance the need for a compact footprint with stringent force and travel range requirements in beam steering and other advanced optical applications.

Introduction

Advancements in silicon photonics have led to a growing demand for Micro-Electromechanical Systems (MEMS) actuators exhibiting high force, broad traveling range, and rapid responsiveness. This demand is especially pronounced in active and tunable photonic devices, where precise control and reconfigurability are essential[1–4]. In recent decades, microsystems have shown their potential in miniaturizing and enhancing the performance of such devices, integrating seamlessly with silicon photonics to create robust and low-power platforms[5,6].

Active photonic systems, such as beam steering devices, tunable lasers, and wavelength-selective switches, require actuators that can generate high force within a compact footprint while maintaining extensive travel ranges. Beam steering, in particular, demands large travel ranges to achieve effective angular deflection and high force intensity to precisely manipulate stiff waveguide structures[4,7–24]. Typically, these stringent requirements entail a traveling range above 1 µm and forces exceeding several milli-Newtons (mN). For beam steering applications involving continuous waveguides[9], the force requirement can reach the range of a few mN with a traveling range of ~5 µm. These constraints make the optimization of MEMS actuators critical, as achieving high force intensity and large displacement without increasing the device footprint is a significant challenge. Our study addresses these requirements by developing and optimizing electrostatic comb drive actuators that enhance force intensity

Correspondence: Muthukumaran Packirisamy (pmuthu@alcor.concordia.ca)
[1]Optical-Bio Microsystems Laboratory, Department of Mechanical, Industrial and Aerospace Engineering, Concordia University, Montreal, QC, Canada

and travel range while ensuring compatibility with space-constrained photonic integrated circuits.

A critical design consideration in the realm of photonic integrated circuits is the selection of an appropriate actuator influenced by the required range of movement, force demands, and power consumption constraints. Electrostatic comb drives, pivotal in many MEMS applications, present optimization challenges due to their high voltage requirements and complex geometry. This includes the number of fingers, their geometry, and the position of movable and fixed beams, all of which significantly impact performance and reliability[4,25–28].

Typically, photonics applications require electrostatic actuators with a small footprint and high reliability, while high force and a large actuation range are needed for some components. Numerous researchers have investigated the optimization of electrostatic comb drives for various applications. Several factors are targeted for optimization, including traveling range[9,29,30], force, actuation voltage, pull-in voltage, and actuator instability. Effective parameters commonly used to improve comb drive performance are the number of comb fingers, electrode spacing, comb structure spring stiffness, and electrode geometry[9,21,22,31–41].

These parameters can generally be classified into two categories: optimizable parameters, which designers can adjust to meet specific requirements, and fixed or system constraint parameters, which are inherent to the system's design and material properties. Understanding these distinctions is vital for achieving the desired actuator performance.

Optimizable parameters

Electrode gap

The electrode gap is instrumental in regulating the force intensity of the actuator. Reducing the gap size enhances the electrostatic forces, thereby increasing force intensity. However, the influence of the gap size on the traveling range is not straightforward and often depends on the geometry of the electrodes. Typically, smaller gaps may result in a reduced traveling range, except in designs like conventional rectangular fingers where the gap size does not directly affect the traveling range. Adjusting this parameter is crucial for controlling the actuator's performance, particularly in terms of force generation, and serves as a primary focus during the design optimization phase.

Finger geometry

Building upon the adjustments in the electrode gap, the geometry of the comb fingers further influences mechanical efficiency and force distribution. Various geometries, such as triangular configurations, can optimize the force per unit area, enhancing how effectively the actuator operates. Modifying the finger geometry provides a means to fine-tune mechanical strength and actuator efficiency, allowing for a tailored balance of these factors to meet specific application needs. This optimization is integral to maximizing the benefits realized from precise electrode gap settings.

Comb and arm configuration

Extending beyond individual finger adjustments, the overall arrangement and assembly of the combs and arms are crucial in defining the mechanical properties and performance of the actuator. By varying this configuration, designers can manipulate aspects such as stiffness and force output, thereby enhancing specific performance metrics. This flexibility in the structural layout allows for comprehensive optimization, aiming to exploit the full potential of adjusted electrode gaps and optimized finger geometries. Such holistic design considerations ensure that the actuator meets precise operational requirements without altering the fundamental material properties of the system.

Fixed or system-constraint parameters

Restoring mechanism

The restoring mechanism, typically a spring-like structure, works in conjunction with the comb frame to return the actuator to its original position after deflection. This mechanism, along with the comb frame that supports the arms and fingers, is critical for maintaining the actuator's stability and reliability. The design specifications for these components are usually fixed to ensure consistent performance, thus limiting opportunities for modifications. Together, the restoring mechanism and comb frame form an integral part of the actuator, essential for its effective operation and mechanical integrity.

Dielectric constant

This parameter is defined by the materials used in the comb drive's construction and influences electrostatic force generation. Alterations to the dielectric constant would require changes in material properties, which may not be feasible within the constraints of current designs.

Driving voltage

The necessary driving voltage is dictated by the overall design and operational needs of the MEMS device. It is considered a fixed parameter as reducing the voltage could undermine the actuator's performance, especially concerning force output and travel range.

In conclusion, while optimizable parameters such as electrode gap, finger geometry, and comb and arm configuration provide flexibility for enhancing actuator performance, fixed parameters like the restoring mechanism, dielectric constant, and driving voltage pose constraints

that must be carefully managed. Striking an optimal balance between these parameters is essential for the development of efficient and reliable MEMS actuators for advanced silicon photonic applications.

Figure 1a provides an overview of the design parameters of comb drives and their impact on performance, underscoring our objective to holistically improve the comb drive configuration and finger geometry design for mechanical actuation in photonic devices. It is important to note that changing each comb drive parameter has pros and cons, depending on the application. For instance, increasing the number of comb fingers to generate more force will increase the overall device footprint, and the comb structure will become more complicated. Alternatively, softening the springs to decrease the driving voltage might cause less lateral instability[34]. Comb drive configuration and finger geometry could be two factors that can improve electrostatic actuator performance without compromising other criteria.

Angled electrodes in electrostatic comb drives

A particularly interesting evolution in designing finger geometry is the advent of tilted angle electrodes, enhancing efficiency and effectiveness in various applications[31,41,42]. This section discusses recent advances and findings in the field, drawing upon a selection of pertinent literature.

In 2015, Gao et al.[34] proposed a double-tilt electrostatic comb-drive actuator for MEMS switches. This actuator has a short overlap length and two tilted finger parts with different tilt angles and reduces pull-in voltage by 25% compared with the rectangular comb-drive actuator. The switching performance was also improved using a tilted parallelogram clamped beam.

In 2019, Bian et al.[32] developed a microswitch using comb drives. A triangular finger geometry is used to increase driving efficiency. Also, integrating the combs into the microcantilever decreases the mass and area of the device and improves the speed response and pull-in voltage.

However, despite these advancements, the intricate interplay between the physical geometry of actuators and their operational efficiency in terms of force, footprint and traveling range has not been extensively explored. This gap is particularly evident in the study by Hoffmann et al.[31], which investigated triangular electrode structures for electrostatic energy harvesting. Their findings indicated that the angle of the electrodes is a pivotal design parameter and that triangular electrodes offer larger capacitance changes per unit displacement and total capacitance change than other designs. Their analysis did not extend to considerations of the footprint and traveling range which are important, especially in the context of silicon photonics, where device miniaturization and efficiency are paramount.

In 1998, Rosa et al.[43] studied the tilted finger geometry and compared it with a regular rectangular finger. It is shown that the force per length of the electrode could increase by controlling the tilted finger angle. However, the effect of finger angle change on the footprint is not considered.

In 1988, Ye et al.[44] showed that using a variable gap design could manage the nonlinear behavior of electrostatic actuators. In fact, the variable gaps will compensate for the nonlinearity often caused by the nonlinear restoring force of comb structures between fingers.

The 2019 study by Phuc Hong Pham et al.[45], marks a significant development in electrostatic comb-drive actuator design by the introducing of the trapezoidal-shaped electrostatic comb-drive actuator (TECA). This design targets higher electrostatic force intensity and greater displacement than the conventional rectangular-shaped actuator. The research offers a detailed analysis of the interplay between beam stiffness and driving voltage in TECA, employing standard SOI-MEMS technology for its fabrication and characterization. While the findings demonstrate TECA's enhanced performance in terms of larger displacement and force intensity. It is notable that their study does not include a comparison or optimization of the actuator footprint and traveling range. This suggests potential areas for further exploration in the context of electrostatic actuator efficiency and application-specific adaptability.

This paper delves deeper into this particular actuator design, aiming to optimize the triangular (TRI) finger geometry to maximize the comb drive actuator's force intensity and traveling range, which is crucial for advanced silicon photonic applications. Our study addresses the intricate interplay between the triangular actuator's physical geometry and operational efficiency, focusing on various design parameters, including the number of fingers per arm, finger dimensions, arm length, and width.

This study advances the field of MEMS actuator design for silicon photonics by providing crucial insights into selecting and optimizing electrostatic comb drive configurations suitable for high-speed, high-force applications. Setting a new benchmark for high-performance photonic integrated circuits, our research offers a detailed roadmap for designing and implementing optimized triangular finger-shape actuators. This work paves the way for more efficient, compact, and powerful photonic systems across various applications, contributing significantly to the development of cutting-edge technologies.

a

Parameter	Force intensity (σ)	Force per traveling range	Parameter type
Electrode gap	+++	+++	Optimizable
Finger geometry	++	++	Optimizable
Comb and arm configuration	+++	+++	Optimizable
Restoring mechanism	+++	+++	Fixed/system constraint
Dielectric constant	+	+	Fixed/system constraint
Driving voltage	+++	+++	Fixed/system constraint

(+) weak effect, (++) moderate effect, (+++) strong effect

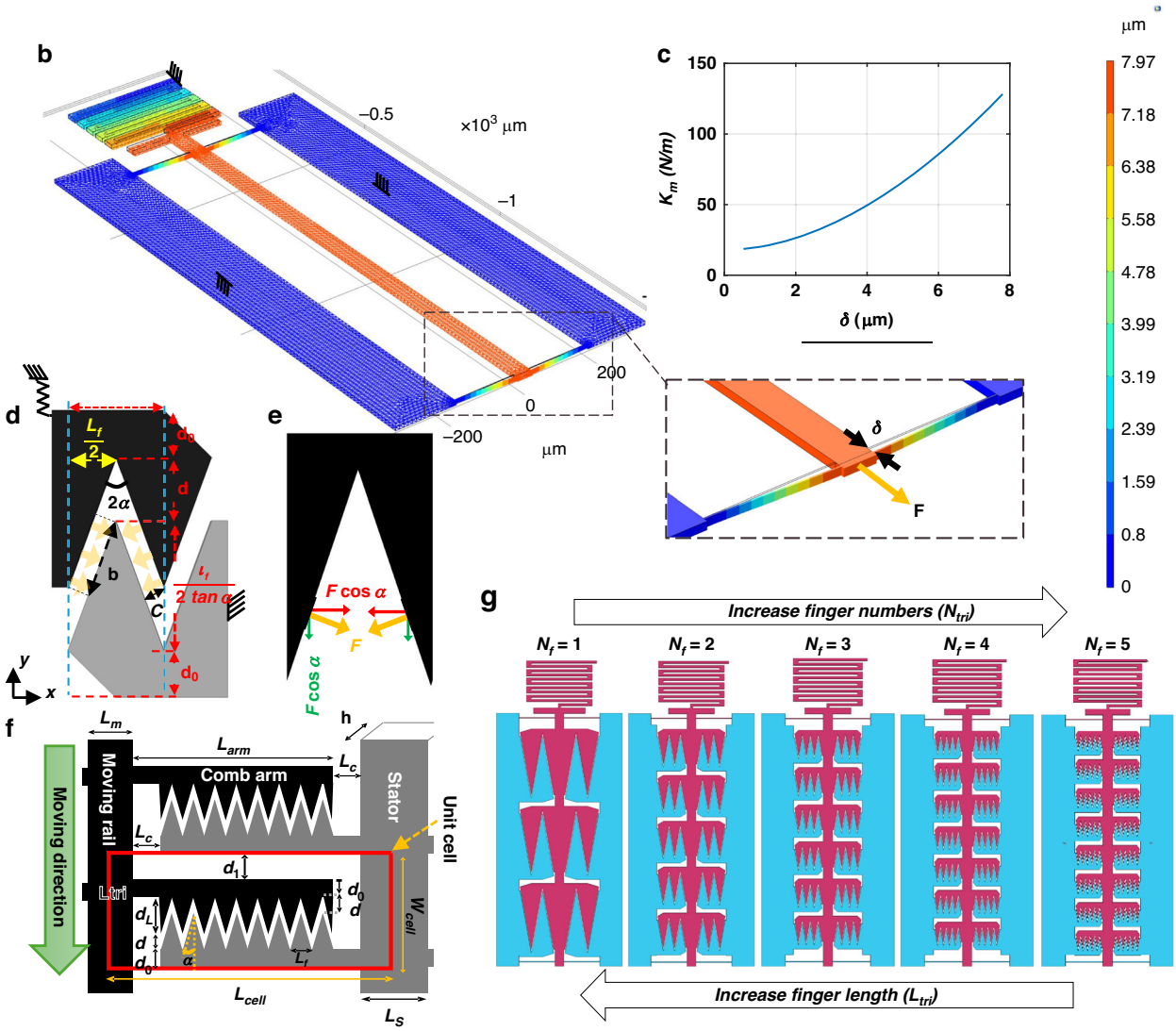

Fig. 1 Design and Performance Characteristics of the Triangular Comb Drive Actuator. a Comb drive design parameters and their impact on comb drive performance[11,31–34,43,48–51]. **b** Finite element analysis (FEA) results highlighting the nonlinear stiffness of the comb drive's mechanical frame for varying configurations. Simulation shows the frame's displacement when force is applied at the moving beam tip. **c** Graph depicting stiffness variation with beam tip displacement. **d** Geometrical configuration of the triangular (TRI) comb finger, showing key dimensions for electrostatic force calculation. **e** Vector decomposition of the electrostatic force. **f** Effect of varying finger count (N_f) and pitch (L_f) on fitting within a fixed actuator area, highlighting geometric adaptability for optimizing force intensity. **g** Detailed view of an electrostatic actuator unit cell with triangular fingers

Results

Structural framework and stiffness considerations

In our pursuit of optimizing the triangular finger comb drive for high-performance silicon photonic applications, a paramount consideration has been the balance between force and the actuator's footprint. We meticulously defined a unit comb drive's support structure adhering to a constant footprint, vital for integrating into compact photonic systems. This framework, consistent in overall stiffness and footprint, ensures practical applicability, where space or footprint efficiency is crucial.

The unit comb drive support structure is designed to achieve low stiffness in the actuation direction while maintaining lateral stability, all within a fixed footprint that allows for consistent evaluation of different finger and arm configurations. This approach ensures that all configurations experience identical mechanical stiffness enabling fair performance comparisons. The structure employs single-beam and serpentine springs, which are designed to minimize restoring forces along the movement path, preventing side pull-in and deformation. The serpentine springs, in addition to their role in mechanical support, also serve as electrical connectors and are strategically positioned to avoid adding unwanted stiffness, preserving the desired displacement range.

This design adheres to parameters outlined in earlier studies, with spring dimensions such as width, length, and placement selected according to the MEMSCAP PiezoMUMPS process[46] design kit for both manufacturability and performance optimization. The serpentine springs (9 μm wide and 293 μm long) and single-beam springs (2 μm wide and 160 μm long) were chosen to meet the minimum fabrication requirements for structures with and without electrical connections, respectively. While the single-beam springs are highly compliant in the actuation direction, they provide substantial lateral stiffness to prevent instability and ensure precise actuation. The moving beam that carries the movable arms is 40 μm wide, ensuring sufficient rigidity to prevent bending along its length, while the stators are designed with a 200 μm width, the minimum required for reliable silicon release to avoid undercut issues during fabrication. The total length of the moving arm or stator is set to 1063 μm.

Our simulations focused on varying triangular finger configurations and respected the constraints of this fixed footprint and stiffness. This strategy enabled us to enhance force intensity while remaining within realistic device size and stability limits. Such attention to detail is critical in evaluating the impact of changes in finger geometry and other parameters on force intensity within our established spatial constraints.

Complementing these design considerations, we conducted simulations to ascertain the unit comb drive framework's stiffness, the key to its mechanical behavior under varying loads. Employing finite element analysis in Comsol Multiphysics, we captured the nonlinear stiffness characteristics intrinsic to MEMS actuators. This process was crucial to understanding how stiffness varies with displacement, a decisive factor in the actuator's operational performance.

To ensure practicality and manufacturability in our design, we aligned our simulations with real-world fabrication constraints, considering minimum dimension requirements and spacing for electrical wiring and structural stability.

In this study, the design adheres to the fabrication constraints outlined by the MEMSCAP PiezoMUMPS process[46], which utilizes a 10 μm Silicon-on-Insulator (SOI) platform. Specifically, the minimum feature size for straight structures is set at 2 μm, while angled designs require a minimum gap of 3 μm to ensure successful patterning and prevent fabrication defects. Additionally, the minimum silicon layer width for free-standing structures is set at 9 μm to ensure adequate structural support and avoid undercut issues. Stator width is defined at a minimum of 200 μm to accommodate deep trenching, while the moving beams and serpentine springs are configured to maintain flexibility and prevent lateral instability. These constraints ensure that the device design is manufacturable and compliant with standard microfabrication processes, preserving both electrical functionality and mechanical stability across all actuator configurations.

These factors played a crucial role in developing a design that was both solidly grounded in theory and practical for production in a MEMS manufacturing setting. The stiffness versus displacement curve, a crucial part of our design process, is detailed in Fig. 1c illustrating the stiffness characteristics of the unit framework under simulated conditions. This figure and our comprehensive simulation approach provide a solid foundation for our optimized design, highlighting the mechanical integrity of our triangular finger comb drive design within the stringent requirements of silicon photonics.

Theory and finger angle selection

In optimizing the design of MEMS actuators, the triangular finger configuration is particularly effective due to its force intensity, a pivotal factor for performance. For the electrostatic force assessment, we initiate by conceptualizing each triangular finger's flank as an inclined segment of a parallel plate system. In commencing our analysis, we dissect the triangular finger's electrostatic forces into their primary components. Figure 1e reveals that the lateral forces along the x-axis from each side of the finger cancel each other. Consequently, it is the components along the y-axis that drive the actuator's motion. This leads us to the equation representing the

force exerted by a single flank of the triangular finger, which is pivotal to our analysis:

$$F = \frac{\varepsilon_0 \varepsilon_r h b V^2}{2c^2} \tag{1}$$

In this expression, F represents the electrostatic force between the parallel plates of one triangular finger flank. The symbols ϵ_0, ϵ_r, h, V, c, and b denote the vacuum permittivity, relative permittivity, electrode thickness, applied voltage, electrode gap, and effective electrode overlap, respectively (Fig. 1d).

The gap between the electrodes, denoted as c, is determined by the vertex half-angle (α) and the distance (d) between the tips of the triangular electrodes. The electrode overlap is defined based on the α, d and finger pitch ($L_{f)}$:

$$c = d \sin(\alpha) \tag{2}$$

$$b = \frac{L_f}{2 \sin \alpha} - d \cos \alpha \tag{3}$$

By integrating the value of c and the electrode overlap b, then incorporating these into the prior equation, we arrive at the following expression for the electrostatic force on each side of the triangular finger:

$$F = \frac{\varepsilon_0 \varepsilon_r h L_f V^2}{2d^2} \left(\frac{1}{2 \sin^3 \alpha} - \frac{d \cos \alpha}{L_f \sin^2 \alpha} \right) \tag{4}$$

Here, L_f indicates the finger pitch. This nuanced equation is the cornerstone for deriving the total driving force F_y:

$$F_y = \frac{\varepsilon_0 \varepsilon_r h L_f V^2}{2d^2} \left(\frac{1}{\sin^2 \alpha} - \frac{2d \cot \alpha}{L_f} \right) \tag{5}$$

The derived equation for the triangular finger force separates into two principal components: the inherent electrostatic force found in parallel plate configurations and an gain factor resulting from the triangular geometry. This factor increases as the electrode angle decreases, improving actuator efficiency within the defined travel range.

Additionally, the triangular finger's design inherently minimizes the space between electrodes, thereby enhancing electrostatic force for certain travel distances. It brings to light how the angle α plays a crucial role in optimizing electrode separation. Fine-tuning this angle, alongside the finger dimensions, allows for precise control over the actuator's travel range, signifying a central aspect of actuator design optimization α in maintaining minimal gaps between electrodes which is a distinctive feature of the triangular design. Adjusting the angle and length of the fingers allows for the customization of the travel range, which is a critical factor in the optimization of the actuator design.

A pivotal aspect of our optimization study is the angle selection for the triangular fingers. Our previous work has shown that reducing the finger angle increases the electrostatic force exponentially, a relationship depicted by a 'gain factor' that compares force amplification against the angle. However, practical fabrication limitations necessitate a minimal angle threshold to prevent the loss of sharp tip features during the etching process. Consequently, an angle of 10 degrees is chosen as it stands on the point of maximizing force intensity while remaining feasible for manufacturing processes. The angle we selected for the triangular fingers strikes a balance between ideal design theory and the realities of manufacturing. This angle leverages the strengths of the triangular shape, notably its capacity to maximize electrostatic force within the chosen movement range, as supported by existing research and practical observations.

The challenge lies in determining the most effective balance between force intensity, traveling range and footprint, ensuring that the triangular finger comb drive achieves the highest performance within the specified design parameters. Our focus on the angle of 10 degrees is rooted in these considerations, striving to optimize the triangular finger design for peak force generation without compromising manufacturing practicality.

Configuration of electrostatic actuator cell with triangular fingers

The electrostatic actuator cell with triangular fingers is defined by a set of parameters that are essential for its design and functionality as shown in Fig. 1g and outlined in Table 1. The element thickness, represented by (h) in our design, is a critical fabrication process constraint that adheres to the silicon layer thickness provided by the SOI technology. Alongside this, the finger separation and stator length are also limited by the precision of the manufacturing process, which dictates the minimum gaps and under-etch tolerances. The triangular finger angle is carefully chosen to balance the need for sharp tips against the risk of losing definition during etching.

Electrode separation along y direction denoted as d, is a dynamic variable tailored to meet the specific traveling range required by the application. It is adjustable within the design to ensure the actuator meets its targeted performance metrics. In this study we have considered d to be 20 μm, with the actual inter-finger gap defined as c in Fig. 1c. However, to ensure reliable and stable actuation, we considered the effective travel range to approximately one-third of this gap, resulting in a design travel range of ~6 μm. This conservative design choice did not account

Table 1 Design parameters and their classification for triangular finger comb drives

Symbol	Description	Type	Limitations	Value
h	Element thickness	FPC	SOI silicon layer thickness	10 µm
c	Finger separation (Dependent)	FPC	$c = dsin(a) \geq 2\ \mu m$	3.51 µm
L_c	Connection beam length between arms and mobile or fixed beams	FPC	$\geq 2\ \mu m$	5 µm
L_s	Stator length	FPC	Deep trench under etch	200 µm
a	Triangular finger angle	FPC	Loosing sharp tips	10.12°
d	Electrode separation along y direction	DV	Proportional to the traveling range	20 µm
d_0	Arm Width	DR	Equal to the arm width	15 µm
d_1	Distance to the next pair of electrodes	DR	Minimize the Electrostatic Force	18 µm
L_m	Moving rail length	DR	Electrode lateral instability	40 µm
D_{max}	Maximum beding deflection	DR	Electrode lateral instability	0.02 µm
L_f	Finger pitch	**OPT**	-	
N_f	Number of fingers in each arm	**OPT**	-	
L_{arm}	Arm Length	DP	$L_{arm} = N_f\ L_f$	
d_L	projected triangular electrodsr's length on Y-axis	DP	$d_L = \frac{L_f}{2\tan a}$	
L_{cell}	Cell length	DP	$L_{cell} = L_{arm} + 2L_c + \frac{1}{2}L_s + \frac{1}{2}L_m$	
W_{cell}	Cell width	DP	$w_{cell} = 2d_0 + d + d_L + d_1$	

This table categorizes the various parameters influencing the comb drive design. Fabrication Process Constrains (FPC) denote fixed values determined by manufacturing capabilities, while Design Variables (DV) are adjustable within design limits. Design Restrictions (DR) are specific DVs with additional limitations, such as maximum bending deflection. Dependent Parameters (DP) are calculated based on other values, and Optimization Parameters (OPT) are those which can be fine-tuned for improved performance. The table helps elucidate the relationships between these parameters, guiding the optimization process for achieving desired force densities and traveling ranges within the structural integrity of the electrostatic actuators

for the non-linear effects in the comb drive behavior, providing a margin of safety.

Certain design restrictions come into play to preserve the structural integrity and operational stability of the actuator. These include the arm width and the distance to the next pair of electrodes, which are crucial in preventing pull-in and lateral instability as well as preventing unwanted electrostatic force between adjacent cells. The moving rail length and the maximum bending deflection are also set within specific limits to maintain the actuator's reliability under operational conditions.

Parameters available for optimization allow for fine-tuning the actuator's performance. The finger pitch and the number of fingers per arm are particularly important as they can be adjusted to maximize force intensity, which is essential for the efficient functioning of the actuator within the desired traveling range.

Finally, dependent parameters such as the arm length, cell length, and cell width emerge as a result of the set constraints and chosen variables. These parameters are computed based on the given values and are integral to defining the actuator's physical geometry, directly impacting its force generation capabilities and mechanical behavior within the compact footprint of silicon photonic devices.

In this paper, we adhere to a unit footprint for comparing different actuator designs, thereby treating the arm length L_{arm} as a design-restricted parameter. It is defined by the equation $L_{arm} = N_f\ L_f$, which aligns the number of fingers per arm and the finger pitch with the constant arm length. This constraint is pivotal to our study, ensuring the comparability of designs by maintaining a consistent footprint across all configurations.

Considering the fact that L_{arm} is constant in this study, adhering to the restriction $L_{arm} = N_f\ L_f$ the number of fingers per arm emerges as the sole optimizable parameter within our design framework. Future work will explore the implications of varying L_{arm} to broaden the scope of optimization and design versatility. This adjustment aims to refine our understanding of how changes in arm length can further influence actuator performance.

As demonstrated in Fig. 1f, with a constant actuator area when finger pitch (L_f) decreases, more fingers (N_f) will be accommodated. However, when L_f decreased the effective electrode overlap will decrease after a point as the d parameter remains constant and there is no electrode overlap at the fingertips. Accordingly, a certain N_f and L_f will form the optimal design for the highest force intensity.

Optimizing triangular finger configurations for comb drives

In our study, the focus is not just on optimizing the force, but on doing so within the constraints of a unit footprint and maintaining a certain traveling range. This necessitates a meticulous examination of the triangular finger geometry in comb drives. By maintaining a constant arm length and exploring the relationship between the number of fingers and their pitch, we aim to maximize force intensity within a defined spatial parameter. Crucial to this effort is the establishment of an optimal arm width, intricately linked to arm length, to mitigate lateral instability in the actuator. The importance of considering the force in a unit footprint means that every geometric aspect of the actuator becomes significant. Therefore, a thorough analysis is required to ascertain the best arm width, in conjunction with a predetermined arm length and electrode thickness. This careful calibration is aimed at preventing the "pull-in" effect, commonly triggered by excessive bending along the arm. Due to small gap spacing between electrodes (c) (starting from ~3.5 μm and decreasing to ~2 μm during the travel range), any lateral movement can significantly alter the gap. When the arm bends, it causes the very end fingers to experience increased lateral deflection, which reduces the effective gap (c) between the electrodes. If this gap is reduced beyond a critical threshold, it can lead to localized pull-in at these specific fingers. This localized pull-in can subsequently trigger a cascading pull-in effect across the entire device. This behavior is distinct from the conventional vertical pull-in seen in parallel-plate actuators and necessitates additional considerations in the design to ensure stability during actuation.

Our methodology not only ensures the structural integrity of the actuator but also optimizes its performance within the specific dimensions of the unit footprint. The design thus balances the need for high force intensity with the limitations imposed by the actuator's physical size, ensuring maximum efficiency and effectiveness in silicon photonic devices.

Arm width optimization for maximum permissible deflection

In line with the primary objectives of our research to optimize force intensity and minimize footprint, we should determine the optimal arm width (d_0) for our triangular finger comb drives. The central constraint for determining d_0 is to ensure it's sufficiently wide to prevent excessive deflection along the length of the arm, which could lead to undesirable side pull-in effects during operation. To ensure operational stability and performance within the allowable deflection limit ($D_{\max}$), it's imperative that the electrode gap remains above the critical pull-in threshold under dynamic conditions. This threshold is defined as two-thirds of the initial gap (c), forming a critical boundary to prevent mechanical failure when the actuator is at its maximum traveling range ($\delta_{\max}$) and the arm is deflected.

The two-third of initial gap threshold originates from the context of linear springs and parallel plate capacitors. However, in our study, this definition is applied to a localized pull-in effect caused by arm bending, primarily affecting the last triangular finger of each arm, which undergoes the most significant deflection (Fig. 2). The nonlinear stiffness of the system results from a combination of the comb drive's restoring force and the arm's cantilever behavior, leading to an overall restoring force that is higher than in the linear case. In such nonlinear systems, the stiffness generally increases with displacement because the stiffness will increase nonlinearly by increasing the displacement (Fig. 1c), making the actual pull-in gap threshold occur at a point smaller than the conventional two-thirds of the initial gap. We have chosen to use the two-thirds threshold as a conservative measure to ensure the design remains stable under worst-case scenarios, as the actual pull-in point would be beyond this threshold due to the increased stiffness.

To determine the relationship between arm width (d_0) and arm length for a given maximum deflection, we have undertaken a detailed study. Each comb finger was conceptualized as a point force exerted at a specific point along the arm, resulting in a deflection (D_i) due to the force from each finger (P_i) (Fig. 2b). This deflection is calculated as follows:

$$D_i = \frac{P_i\, b_i^2}{6\,E\,I}(3L_{arm} - b_i) \tag{6}$$

$$I = \frac{1}{12} h\, d_0^3 \tag{7}$$

Where b_i represents the distance from the arm anchor to the center of the i^{th} finger, E is the modulus of elasticity, reflecting the silicon stiffness and I is the second moment of inertia, indicating the beam's resistance to bending, calculated here for a rectangular cross-section based on the arm's thickness (h) and width (d_0). For an arm with multiple fingers, the overall deflection, which we refer to as $D_{\max}$, is the sum of the deflections caused by each finger:

$$D_{\max} = \sum_i \frac{P_i\, b_i^2}{6\,E\,I}(3L_{arm} - b_i) \tag{8}$$

By plotting the relationship between arm width and arm length for different acceptable deflections, as illustrated in Fig. 2d, we can determine the necessary arm width for the desired arm length and maximum deflection.

Our calculation baseline to determine the $D_{\max}$ was chosen conservatively, based on the configuration most

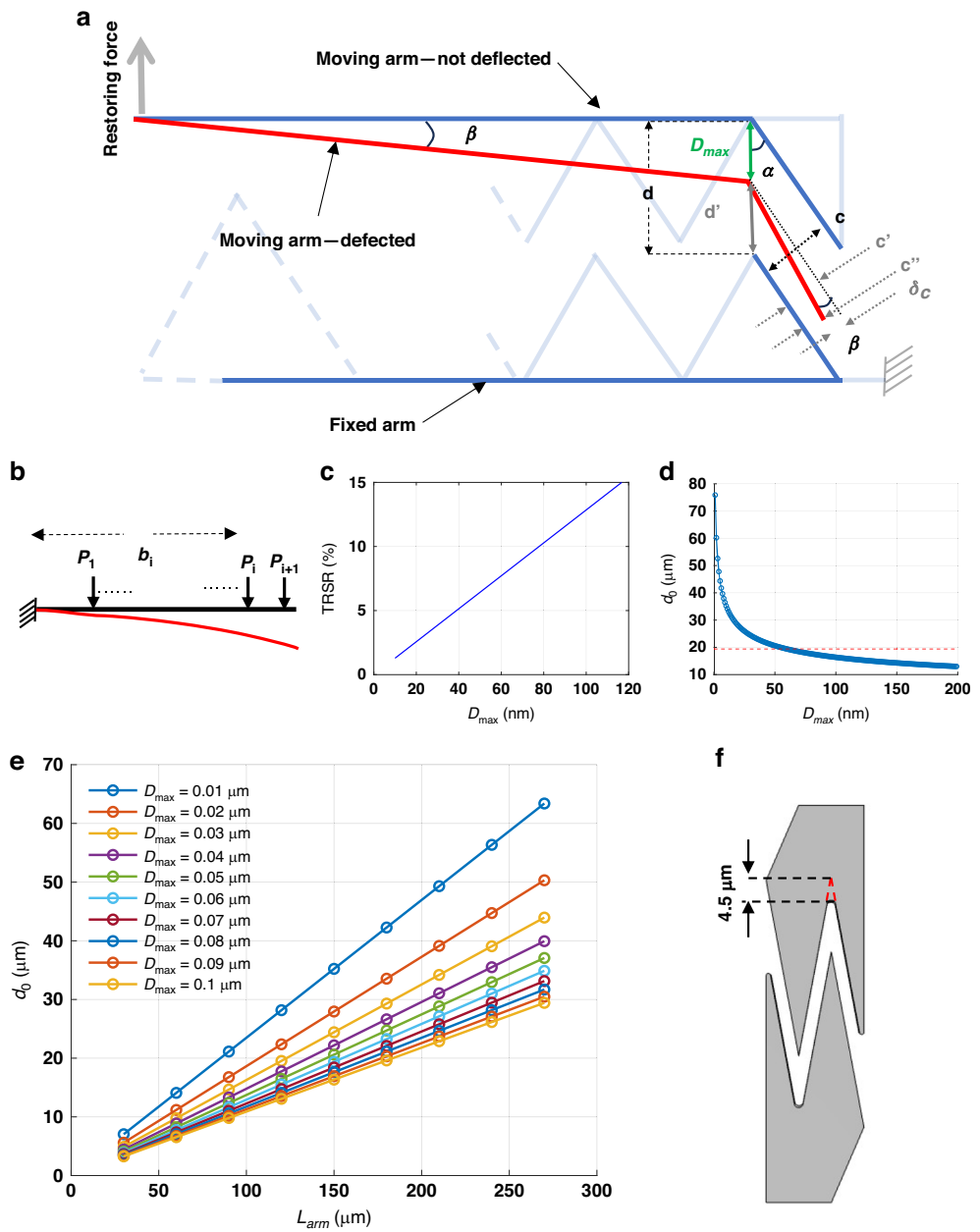

Fig. 2 Analysis of arm deflection in triangular finger comb drives. a comparison of the moving arm in its undeflected and deflected states, delineating the arm's movement due to applied restoring force and showing the reduction in the gap (c to c' to c''). The red line represents the arm's deflected state, with β denoting the deflection angle, and d' indicating the reduced electrode gap due to bending. **b** Schematic of force application on the arm, with P_i indicating the point force applied by the i^{th} finger at distance b_i from the anchor point, resulting in the deflected profile (red dashed line). **c** This graph shows the linear correlation between the maximum deflection (D_{max}) in nanometers and the Travel Range Sacrifice Ratio (TRSR) in percentage. As D_{max} increases, TRSR also increases, depicting the trade-off between actuator deflection and travel range reduction. **d** Required arm width vs. maximum permissible deflection (D_{max}) for arm length of 150 μm. The red line marks the chosen D_{max} of 60 nm, corresponding to a TRSR of 7%, balancing compactness and travel range. **e** Graph plotting the relationship between arm width (d_0) and arm length (L_{arm}), with various curves representing different maximum permissible deflections (D_{max}). **f** The modified arm design, depicted with a chamfered profile that mitigates stress concentration and increases the stiffness of the arm, is a strategic modification for fabrication considerations. This design adjustment specifically addresses manufacturing challenges associated with sharp corners and enhances the overall mechanical stability of the structure

susceptible to gap reduction upon arm deflection—a single triangular finger per arm ($N_{tri} = 1$). To assure the reliability of the actuator, we identified a deflection gap (c''), which is the remaining gap at the actuator's maximum travel range while the arm is deflected. This gap was determined to be greater than the pull-in threshold, thereby ensuring that the gap remains safely above this essential margin even when the arm is fully deflected.

Figure 2a illustrates a direct comparison of the arm's position, both undeflected and deflected, a critical analysis for understanding the electrostatic interactions within the comb drive. Initially, the electrode gap (c) without deflection is expressed as:

$$c = d\sin(\alpha) \tag{9}$$

Post deflection, this gap reduces to c' and c'' where c' signifies the reduction purely from $D_{\max}$:

$$c' = d'\sin(\alpha) \tag{10}$$

$$d' = d - D_{\max} \tag{11}$$

For c'', which considers the gap's further reduction due to the arm's angle shift, we calculate δ_c, the gap decreases from the electrode tilt as a result of deflection. Using simple angular geometry and approximating $\tan(\beta) \approx \sin(\beta)$, we derive the following relationship for δ_c :

$$\delta_c \approx \frac{D_{\max}}{2\sin\alpha} \tag{12}$$

Consequently, c'' is determined by:

$$c'' = c' - \delta_c \tag{13}$$

To calculate the maximum allowable deflection, we assume that the actuator has already moved one-third of the electrode distance ($\delta_{\max}$), which is defined as follows:

$$\delta_{\max} = \frac{1}{3}d \tag{14}$$

Therefore the d' at $\delta_{\max}$ would be :

$$d'_{\delta_{\max}} = d - \delta_{\max} - D_{\max} \tag{15}$$

And inserting values for c' and δ_c for the $\delta_{\max}$ traveling range yields:

$$c''_{\delta_{\max}} = (d - \delta_{\max} - D_{\max})\sin\alpha - \frac{D_{\max}}{2\sin\alpha} \tag{16}$$

From the equations, it is clear that when the displacement reaches $\delta_{\max}$, ideally $D_{\max}$ should be zero to prevent side pull-in effects. However, bending in the arm is an inherent issue. Consequently, we need to determine how much reduction in $\delta_{\max}$ is acceptable to accommodate some deflection, $D_{\max}$. This approach involves a trade-off where reducing the travel range of the actuator (by adjusting $\delta_{\max}$) allows for a certain amount of deflection ($D_{\max}$) without necessitating an increase in arm width (d_0). This compromise helps manage the physical dimensions of the actuator effectively, termed as the travel range sacrifice ratio (TRSR).

The TRSR quantifies the percentage of the initial gap between electrodes that is consumed due to arm deflection at the actuator's maximum traveling range. Mathematically, TRSR is given by (see Fig. 2):

$$TRSR = \left(1 - \frac{c''}{\frac{2}{3}c}\right) \times 100 \tag{17}$$

where c is the initial gap, $\frac{2}{3}c$ is the conventional threshold for pull-in, and c'' is the final gap between electrodes after accounting for arm bending. This metric essentially captures how much of the critical pull-in threshold gap is used up as the actuator reaches its maximum travel range, thereby indicating the level of safety against pull-in failure. By utilizing TRSR, we can evaluate the trade-off between the desired travel range and stability of the actuator. To select an optimal TRSR, we examined the relationship between the arm width (d_0) and the maximum permissible deflection ($D_{\max}$), depicted in Fig. 2d. This graph demonstrates that the arm width must increase exponentially if a very low $D_{\max}$ is chosen. This graph shows that for $D_{\max}$ less than 60 nm the corresponding arm width becomes impractically large however it does not gain too much on the TRSR based on Fig. 2c. Therefore we select 7% TRSR witch is corespond to 60 nm maximum arm deflection and 19.5 um arm width that allows for a reasonable arm width increase without severely affecting the actuator's mechanical footprint.

To accommodate the challenges of sharp concave corners encountered during the microfabrication process, the arm design was modified to incorporate rounded corners at these crucial points. This modification effectively increases the arm width (d_0) by an additional 4.5 µm (Fig. 2e). As a result, the initial design specification of the arm width was revised from 15 µm to a fabricated width of

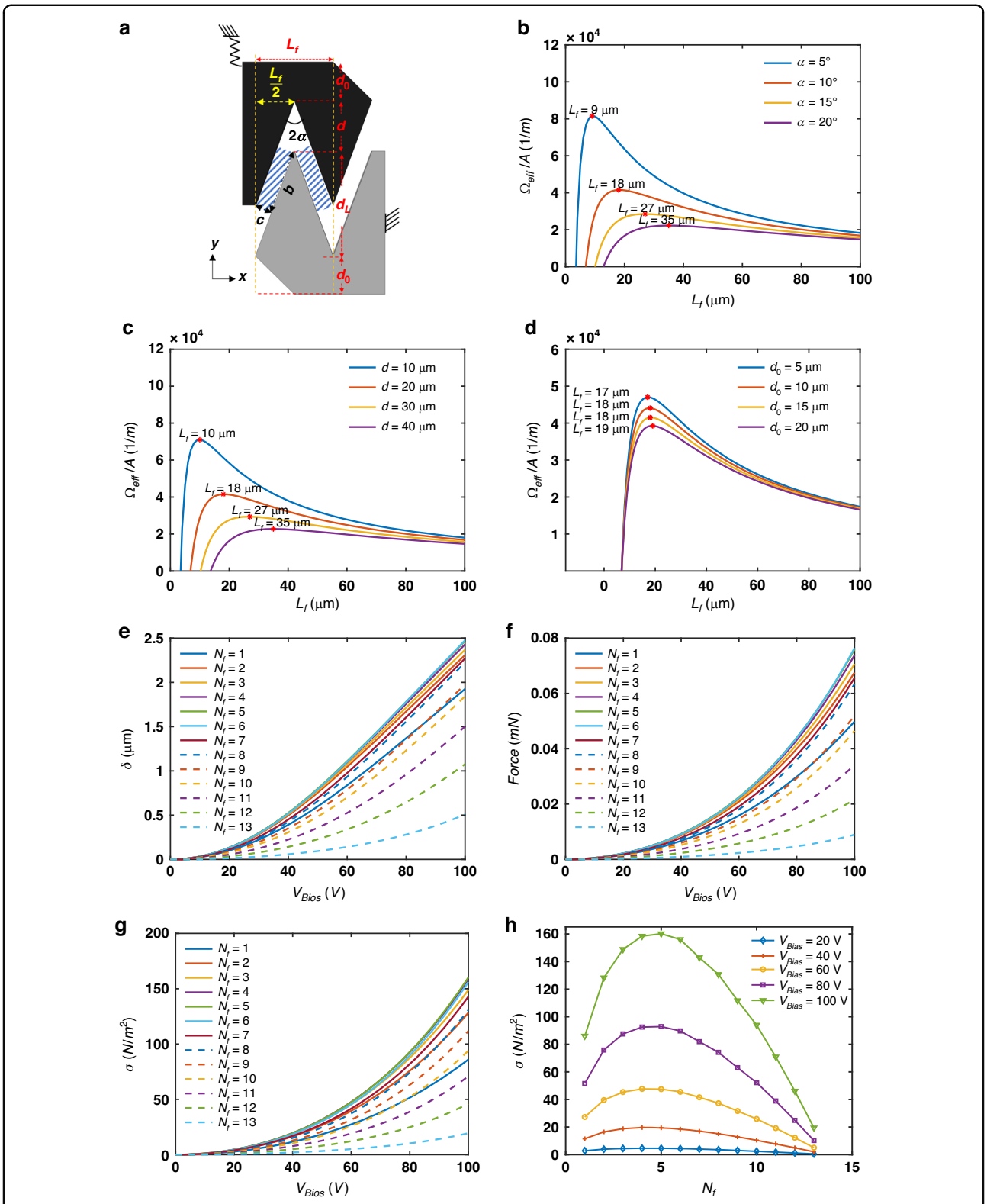

Fig. 3 (See legend on next page.)

(see figure on previous page)
Fig. 3 Parametric and Analytical Evaluation of Triangular Comb Drive Electrode Performance. a–d shows the parametric influence on effective electrode length in triangular comb drives. **a** Unit cell highlighting dimensions for electrode length calculation. **b** Effect of finger pitch (L_f) on electrode length across varying finger angles (α). **c** Impact of travel range on electrode overlap. **d** Influence of arm width (d_0) on electrode length, with optimal pitch marked by asterisks for design optimization. **e–h** shows the analytical models of triangular finger comb drive performance. **e** Graph depicting displacement versus voltage for triangular finger comb drives with varying finger numbers (N_f), illustrating the relationship between applied voltage and the resulting displacement of the actuator. **f** Force intensity versus voltage for different finger counts, demonstrating how the electrostatic force intensity scales with voltage and finger number. **g** A plot of force intensity versus voltage for various numbers of fingers. **h** Force intensity as a function of the number of fingers per arm for different voltages, highlighting the optimization of force intensity with the geometry of the comb drive

19.5 µm, ensuring that our theoretical calculations align accurately with the arm's dimensions after manufacturing

It is also important to consider that the actual stiffness of the arm, due to the triangular fingers' added, the second moment of inertia of the arm will be greater than what a simple cantilever model would suggest. Therefore, by selecting $D_{\max}$ at 60 nm and including a 7% TRSR, we accommodate for more than the cantilever's simple stiffness, resulting in a more robust arm that maintains a safe electrode gap, thereby mitigating the risk of side pull-in across all configurations examined in our study.

In our investigation, we have carefully tailored the arm width within triangular finger comb drives to enhance force intensity while conforming to fixed footprint and travel range constraints. This task extended to ensuring reliable operation within set deflection limits ($D_{\max}$), with an emphasis on maintaining the electrode gap beyond the pull-in threshold to prevent mechanical failure during operation.

Parametric analysis of electrode overlap in triangular finger comb drives

To improve electrostatic actuator performance, understanding the effective electrode overlap is critical as it is directly proportional to the electrostatic force generated in a comb actuator of a given footprint. The intricate relationship between finger geometry and overlap efficiency is captured in our parametric study, which is crucial for optimizing the comb drive configurations for silicon photonic applications.

The effective electrode overlap per unit area is a pivotal metric in assessing the comb drive's force output potential. As shown in Fig. 1f, in a unit footprint as the L_f decrease there is more electrode overlap as the number of figures per unit footprint increases. However, we should consider that there is no electrode overlap at the fingertip due to increased non-overlapping fingertip areas governed by the travel range (d) and the finger angle (α). Therefore, decreasing the L_f could increase the effective electrode overlap, which means electrode overlap minus the fingertip part, up to a certain threshold. After a maximum electrode overlap length, the effect of the electrode tip will be dominant.

The effective electrode overlap for each finger would be two times the electrode overlap at each side of the triangular finger (see Eq. (3)). The following equations provide a mathematical foundation for calculating effective electrode overlap (Ω_{eff}) :

$$\Omega_{eff} = 2\,b \tag{18}$$

According to the Fig. 3a, the area of one single finger (A) would be:

$$A = L_f d_L + L_f\, d + 2L_f\, d_0 \tag{19}$$

Then using Eq. (3) and Eq. (18) and replacing d_L from Table 1 the effective electrode overlap per area that finger occupied would be:

$$\frac{\Omega_{eff}}{A} = \frac{\frac{L_f}{\sin(\alpha)} - 2d\cos(\alpha)}{\frac{L_f^2}{2\tan(\alpha)} + L_f\, d + L_f d_0} \tag{20}$$

The effective electrode overlap, denoted as Ω_{eff}, is the measure of electrode length that actively contributes to the electrostatic force, discounting the length at the fingertips that do not overlap due to the design of the actuator. In Eq. (20), the finger pitch, L_f, is the spatial frequency of the fingers within the comb drive, influencing both the intensity of electrostatic interactions and the physical robustness of the device. The variable d, representing the separation between fingertips, directly correlates with the actuator's travel range, defining the maximum extent of deflection permissible without pull-in. The half-angle of the finger, α, shapes the geometry of the triangular fingers, thereby affecting the electrostatic force and the overall efficiency of the actuator. The arm width, d_0, ensures the mechanical stability of the moving parts and dictates the maximum allowable deflection to prevent Pull-in. Lastly, A, the actuator area, encapsulates the total operating region of the electrostatic interactions.

These equations facilitate the computational analysis required to determine the optimal comb drive design that harnesses maximum electrostatic force within the constraints of silicon photonic device footprints.

Figure 3a represents the unit cell, highlighting the critical dimensions influencing the effective electrode length. This dimensioning sets the stage for understanding how geometry modifications affect force generation. Figure 3b displays the relationship between the finger pitch (L_f) and the effective electrode length per actuator area for different angles (α). The peaks of the curves shift leftward as the angle decreases, suggesting that sharper angles favor a smaller finger pitch to maximize the effective electrode length. For instance, at an angle of 5°, the optimal L_f is significantly smaller compared to an angle of 20°, where the peak is at larger L_f, demonstrating that steeper angles are more sensitive to changes in finger pitch. Figure 3c shows the dependency of the effective electrode length on finger tip-to-tip separation (d), which is directly proportional to the travel range. Each curve peaks at a different L_f value, with a notable trend. As d increases, the peak shifts towards a larger L_f. This indicates that larger travel ranges require a less dense finger configuration to maintain high electrode overlap. Figure 3d illustrates the impact of arm width (d_0) on the effective electrode length. The peaks are very close to one another, but a trend can be discerned where larger d_0 values slightly shift the optimal L_f to a higher value. This subtle shift implies that while arm width does have an effect, it is less pronounced compared to the travel range or finger angle.

Each curve in the graphs is marked with an asterisk at the point of maximum electrode overlap, signaling the ideal finger length (L_f) for each operational parameter. This visual signal guides the optimization of finger pitch in relation to finger angle, travel range, and arm width, which is crucial for maximizing electrode overlap and electrostatic force within the device's footprint. These insights facilitate precise tuning of the comb drive's design, enabling the achievement of optimal force intensity within its operational envelope.

Analytical calculation of traveling range and force intensity of triangular finger comb drives

In this section, we provide detailed analytical calculations for a parametric study on the force intensity of triangular finger comb drives, while maintaining the desired traveling range. These calculations form the basis for optimizing the actuator design, ensuring that each parameter is tailored to enhance performance within manufacturable criteria. This approach ensures that the design not only meets the rigorous demands of optical MEMS applications in silicon photonics but also adheres to practical fabrication limitations, promoting both feasibility and efficiency in production.

In the analysis presented in this section, we build upon the theoretical framework established earlier in this paper to calculate the analytical results. Utilizing the derived equations for the electrostatic force exerted by triangular finger comb drives, specifically Eq. (5), we quantitatively assess the force intensity under varying design parameters while maintaining the required traveling range.

The traveling range of the comb drive is intrinsically linked to its mechanical stiffness, characterized numerically (Fig. 1c). The interplay between the mechanical restoring force and the electrostatic force establishes the actuator's maximum traveling range.

Simulation considerations for enhanced precision in MEMS design To enhance the precision of our analytical model, we incorporated several key considerations into our MATLAB simulation process. Firstly, we utilized COMSOL Multiphysics for the numerical calculation of the comb structure's mechanical stiffness across its entire displacement range. This involved deriving mechanical force values at various points, achieved through interpolation of the data obtained from COMSOL simulations. Such an approach ensures a comprehensive understanding of the comb drive's mechanical behavior under various operational conditions.

Further refining our model, we accounted for the electrostatic forces existing between adjacent cells of the comb drive. This includes a detailed analysis of the interactions between moving and stationary parts of each cell, which is critical for accurately predicting the actuator's performance. Additionally, our model accommodates the inclusion of half a triangular finger in the count of fingers per arm. This design consideration allows for greater flexibility in the actuator design, facilitating the maintenance of a constant arm length while accommodating an integer number of fingers. Moreover, the displacement within the comb drive is calculated by finding the equilibrium point where the electrostatic force balances with the mechanical force. This equilibrium point is pivotal in determining the actuator's operational efficiency and reliability.

Finally, our model incorporates the fringe field effect, as quantified by the Palmer formula[47]. This inclusion is particularly important in scenarios where fringe field effects are pronounced, thereby enhancing the accuracy of our electrostatic force calculations and providing a more realistic representation of the comb drive's performance. These enhancements to our MATLAB simulation framework are instrumental in achieving a more accurate and reliable analytical model, essential for optimizing the design and functionality of triangular finger comb drives in optical MEMS applications.

Analytical results overview In Fig. 3e, f, which presents the results of the analytical models of triangular finger comb drives' performance, we illustrate the relationship between various design configurations and their operational characteristics. It is crucial to emphasize that the

results shown in Fig. 3e, f, similar to those in Fig. 3g, h, are derived using the specific design parameters detailed in Table 1. For consistency in performance evaluation, the results presented in Fig. 3e focus on 0–100 V range corresponding to the 0–2.5 μm displacement range, which is within the stable operating regime for all configurations. This displacement range was chosen to facilitate a direct comparison of force intensity trends across different configurations while avoiding variations caused by differences in pull-in voltage or maximum travel range. Although each configuration can achieve larger displacements depending on the applied voltage, this range captures the performance in a controlled manner, suitable for optimization and benchmarking. To further expand on the travel range performance, a pull-in study is provided in Fig. 7g, h showing the maximum travel range for each configuration and the corresponding voltage required. This analysis highlights that while all configurations can reach similar maximum displacements, the designs with higher numbers of fingers achieve these displacements at significantly lower voltages, demonstrating their improved efficiency and suitability for precision actuation.

Figure 3e, illustrates that, particularly near five fingers per arm, comb drives exhibit a nonlinear to linear transition in displacement response as voltage increases. The linear response observed near five fingers per arm results from the interaction between the non-linear restoring force of the comb drive structure and the exponential growth of the electrostatic force generated by the triangular fingers. The restoring force, influenced by the stiffness of the frame, increases non-linearly with displacement. In contrast, the triangular fingers produce a variable electrostatic force that rises exponentially with displacement, which can be adjusted by the number of fingers per arm. By varying this parameter, we identified configurations (like five fingers per arm) where these opposing non-linear effects are balanced, leading to an approximately linear force-displacement behavior. This linearity is maintained up to the pull-in voltage of the design.

This optimal finger count allows for greater displacement at a given voltage, indicating a design sweet spot for maximizing efficiency. Such behavior is critical for applications requiring precise actuation, as it suggests the need to operate above the voltage threshold where displacement becomes predictably linear, thus ensuring accurate control of the actuator's movement. An exemplary application in silicon photonics where this characteristic is especially beneficial is in tunable optical filters. These filters, essential in wavelength division multiplexing systems, rely on finely-tuned mechanical actuation to adjust their passband for selecting specific wavelengths. The linearity of actuator movement in such devices is pivotal, ensuring predictable and precise adjustments of optical elements, which directly translates to accurate wavelength control. This is particularly crucial in high-speed optical communication networks where precise wavelength tuning and stability are essential for efficient and interference-free signal transmission.

In Fig. 3f, g, the trend lines exhibit how force and force intensity scale with increasing voltage for various finger configurations. Notably, all configurations share a similar pattern of growth, with force and force intensity progressively rising as voltage is ramped up. However, as shown in Fig. 3e, the selection of the operating voltage should consider the requirement for linear displacement within the application's specific performance parameters. Additionally, the variation in finger counts leads to distinct force and force intensity characteristics, as elaborated in Fig. 3h. Such variations must be judiciously considered in the context of application-specific demands, like linearity and desired force levels, to achieve optimal actuator operation. A pertinent example in silicon photonics is the implementation of MEMS-based Variable Optical Attenuators (VOAs). These devices require precise control of attenuation levels, which depends directly on the linear response of the actuator to the applied voltage. The variation in finger counts leads to distinct force and force intensity characteristics. Such for managing signal strengths in optical variations must be carefully considered in the context of VOAs, where the linearity in the actuator's movement and the corresponding force levels are critical for maintaining consistent attenuation across different channels. This ensures optimal operation of the VOAs, which is vital in communication networks, thus enhancing the overall efficiency and reliability of the system.

Comparing analytical models with electrode overlap analysis Figure 3h offers a robust confirmation of our analytical predictions, reflecting the optimal design parameters previously established in Fig. 3a–d. Within the confines of our unit footprint, our design strategically accommodates an integer number of fingers, inherently causing variations in arm's length across different configurations; yet it is the average arm length of ~110 μm that emerges as a standard in our models. This length, when paired with the optimal finger pitch of 18 μm identified in Fig. 3a–d based on the design parameters outlined in Table 1, results in a design that accommodates around six fingers per arm. While this number slightly differs from the peak force intensity indicated at 5 fingers per arm in Fig. 3e–h, this variation can be attributed to the different theoretical approaches used in each analysis. Figure 3a–d focuses primarily on the effective electrode overlap, which is a key factor in the electrostatic force generation. However, Fig. 3e–h incorporates a more comprehensive analytical model, considering both the

electrostatic force calculations specific to the triangular electrode geometry and the numerically derived mechanical restoring force. This comprehensive approach in Fig. 3e–h may lead to a slightly different optimal finger count due to the inclusion of additional factors that affect the actuator's performance. These differences between theoretical models show how complex it is to optimize MEMS comb drive designs, as they require considering many interacting physical factors at once to get the best performance. As we have demonstrated through rigorous analytical calculations and studies in this section, our model provides valuable insights into the performance of triangular finger comb drives. In the upcoming sections, we will delve into numerical results, further enriching our understanding and paving the way for comprehensive advancements in MEMS actuator performance.

Numerical simulation and analysis

To confirm our analytical calculations, we ran a simulation using the Finite Element Method (FEM) in COMSOL Multiphysics 6.0. This approach allowed us to make sure our predictions about the comb drive were accurate. The simulation setup was comprehensively configured to accurately model the behavior of the triangular finger comb drives. Key components of the setup included:

- Geometry Configuration: The geometry was meticulously designed to mimic the real-world structure of the comb drives, with particular attention to the chamfered design of the new arm, ensuring a realistic simulation of physical interactions.
- Material Selection: Silicon was chosen as the primary material for the electrodes, considering its prevalent use in MEMS technology. Air, serving as the dielectric medium, was accurately modeled to capture electrostatic interactions. The mechanical and electrical properties of the materials are obtained from the COMSOL library.
- Physics Interfaces: The model utilized a combination of solid mechanics, electrostatics, moving mesh, and electromechanical force physics to capture the complex interplay of mechanical and electrical forces in the device.
- Mesh Configuration: The entire model was meshed with tetrahedral elements, with careful sizing to balance accuracy and computational efficiency. Initial Mesh sizing is 7.75 μm for maximum element size, 0.56 μm for minimum mesh size, and 1.4 for maximum growth rate (Fig. 4).
- Parametric Sweep and Study Settings: The study conducted a detailed parametric sweep, varying the number of triangular fingers per arm from 1 to 15. This allowed for a comprehensive analysis of how the number of fingers impacts the actuator's performance.

In the numerical simulations depicted in Fig. 4a, we analyze the electric field norm (the magnitude of the electric field vector, measured in volts per meter (V/m)) across a selection of finger configurations within the triangular finger comb drives, focusing on understanding how the electric field intensity distribution varies with different designs. The simulations were conducted for a series of comb drives with finger counts ranging from $N = 1$ to $N = 15$, with $N = 2$, 4, 6, 8, 10, and 15 specifically illustrated to showcase the trend across the spectrum.

The results demonstrate a clear trend: as the number of fingers increases, there is an initial enhancement in the electrostatic force, as indicated by the more intense coloration representing higher electric field norms. This increase suggests that a greater number of fingers can enhance the overall electrode overlap area per unit area, potentially up to a certain point. However, the trend does not continue indefinitely. Beyond a certain number of fingers, the force intensity does not increase proportionally and may begin to plateau or even decline. This observation points to the influence of non-overlapping fingertip areas, which grow more significant as the number of fingers

increases, eventually impacting the effective overlap area and thus the electrostatic force generation.

The color gradient in the electric field norm—from blue, indicating lower intensity, to red, showing higher intensity visually represents the electrostatic forces in action. A peak in the gradient occurs at intermediate finger counts before the gradual decline, suggesting an optimal range of finger configurations for maximizing force intensity within the design constraints. This complex relationship highlights the importance of balancing finger geometry to optimize electrostatic force generation within the comb drive design, without committing to a specific optimal number of fingers but rather identifying a favorable range that aligns with the trends observed in the analytical calculations.

Figure 4c–e presents the numerical simulation results for the triangular finger comb drives, highlighting three essential performance metrics. These results are critical for corroborating the analytical models discussed earlier in the paper. Figure 4c confirms a consistent increase in displacement with voltage across all finger configurations, affirming a direct correlation between the mechanical response of the actuator and the applied electrostatic forces. This trend aligns with our analytical predictions, substantiating the model's applicability across various operational conditions. Figure 4d, depicting the force versus voltage, shows an upward trend for all finger counts, suggesting an increase in force with voltage.

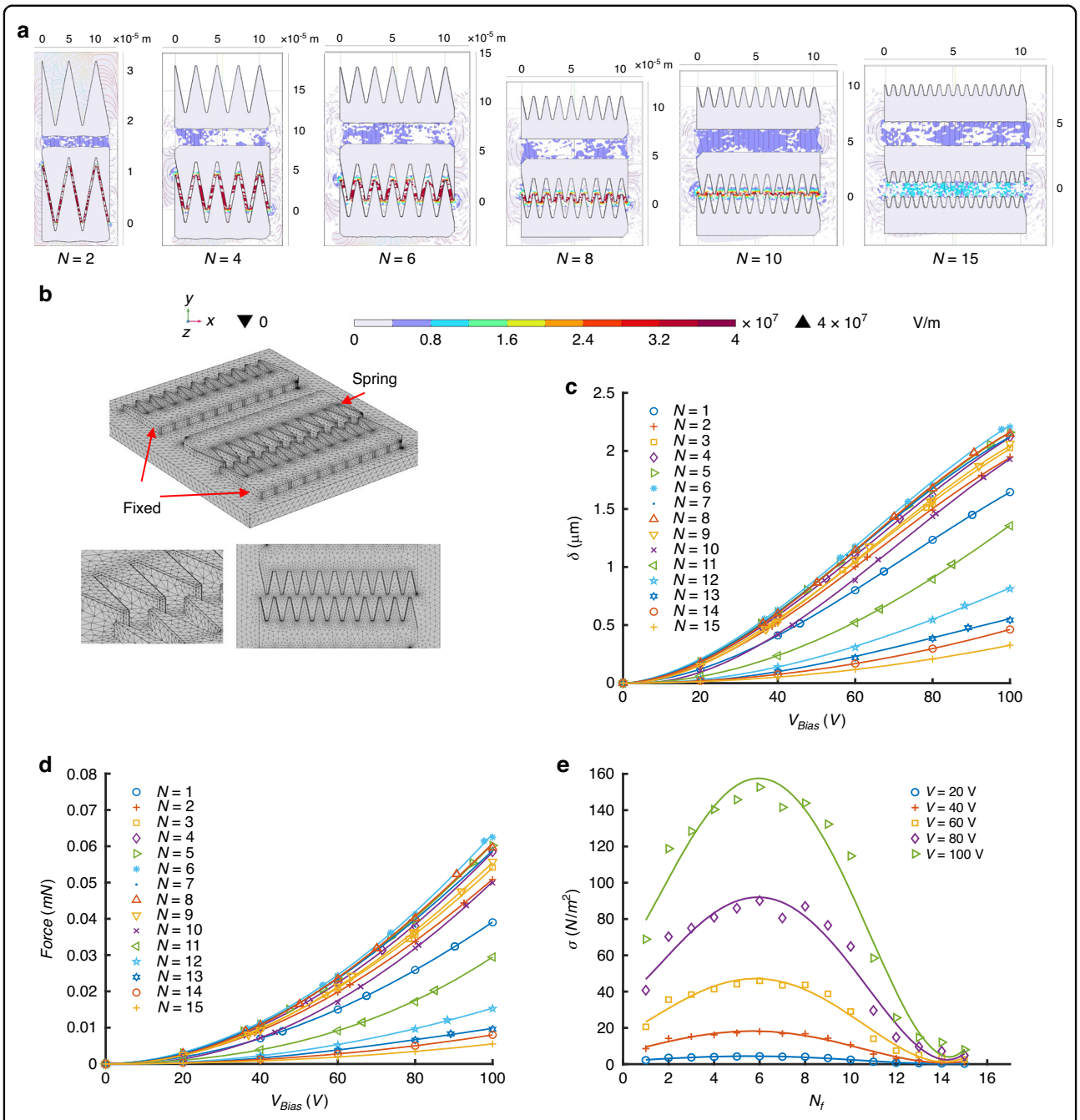

Fig. 4 Electric Field Distribution and Performance Metrics of Triangular Comb Drive Actuators. a Electric field norm distribution across various triangular comb drive configurations ($N = 1, 2, 5, 10, 15$), with color gradients indicating field intensity (V/m) **b** FEM simulation of a MEMS comb drive, illustrating the overall device structure, including adjacent arms, fixed and spring boundaries, and chamfered edges to reduce sharp-edge effects. **c**–**e** Numerical simulation results for triangular finger comb drives**. c** detailing displacement vs. voltage, **d** force vs. voltage, and **e** force intensity vs. number of fingers per arm. The hollow circles represent the actual data points obtained from the simulations, while the solid lines are the fitted curves that provide a visual guide to the underlying trend of the data. These results highlight the actuator's performance metrics, with a peak in force intensity observed near $N = 6$ fingers per arm, indicating an optimal balance for actuator efficiency across various voltage levels

Figure 4e, which plots force intensity against the number of fingers per arm, indicates an optimal range for finger configurations that maximize force intensity. The numerical simulations suggest the maximum force intensity occurs near $N_f = 6$ which is aligned with the analytical model based on the electrode overlap. However, the analytical model based on the calculation of the electrostatic force and restoring mechanical force

indicated $N = 5$. This slight variation is within the expected range given the differences between the theoretical and numerical approaches. Such discrepancies can be attributed to the greater detail and complexity accounted for in the numerical simulations, which include factors such as electrode edge effects and finger-tip effects that are not as pronounced in analytical calculations. This small change in the best number of fingers doesn't change the overall pattern, which both methods confirm.

In summary, the numerical simulations support the analytical findings, with both approaches indicating a similar trend of increasing force intensity up to a point before it decreases. The numerical results suggest this peak is slightly beyond $N_f = 5$, which may influence the final design decisions for actuators where the precise number of fingers is a critical parameter. Such insights will inform future optimizations and design iterations, ensuring that MEMS actuators are tailored to their specific application requirements with the highest degree of accuracy.

Experimental validation

To corroborate our theoretical and numerical findings, we conducted experimental validations of the triangular finger comb drives with varying numbers of fingers per arm ($N_f = 1$ to $N_f = 5$). These experiments were crucial for testing the real-world applicability of our models and understanding the actual performance characteristics of the comb drives in a physical setting.

Fabrication results

In our comprehensive analysis of MEMS comb actuators, we used SEM imaging to examine the minute architectural decisions that significantly impact performance. Figure 5b–h affords us a detailed visualization of these actuators at the microscale.

Section (b) offers a top-down overview, revealing a series of actuators with incrementally increasing finger counts, essential for comparing performance metrics across designs. Section (c) delves into the design of the single beam spring mechanism, captured at a 45° angle, which is pivotal for the actuation process, providing the necessary tension and flexibility for the moving parts. Section (d) provides a closer examination of the suspended silicon layer's thickness from a similar angle, an important factor in the actuator's mechanical resilience and electrostatic functionality.

In section (e), the actuator with four fingers per arm is scrutinized, demonstrating the precise arrangement that facilitates controlled movement and robust performance. Section (f) displays a close-up view of the actuator's top springs and their serpentine configuration, which are not only mechanically strategic but also critical for ensuring consistent electrical connectivity.

Adjacent to these springs, the vernier scale is placed, a feature paramount for quantifying the actuator's micromovements with high accuracy. Section (g) looks underneath the actuator, showing the foundational single beam springs from an angle that provides insight into the structural underpinnings of the actuator's mobility. Finally, section (h) zooms out for a broader perspective, placing the actuators with one and two fingers per arm side by side.

The SEM analysis was critical for verifying the fabrication quality of the MEMS actuators, ensuring that both mechanical structure and electrical connections met our stringent design requirements. This level of scrutiny is vital for confirming that the actuators perform reliably in their silicon photonic applications, where precision is paramount.

Experimental results

The experimental data for our MEMS comb drives with triangular finger configurations are presented in Fig. 6a which plots displacement against voltage for devices with one to five fingers per arm. The trend exhibited by the measured displacement is in general agreement with our theoretical predictions and numerical simulations, indicating a successful translation of the design principles into practice. However, a notable observation is the increased displacement for a given voltage across all configurations when compared to the theoretical and simulated models. This discrepancy suggests a more responsive actuator behavior in the fabricated devices. To provide a quantitative assessment of the proposed design, Figure 6h presents a comparative analysis of critical performance metrics, including traveling range, electrostatic force, and device footprint. The data underscore the advantages of the triangular comb drive configuration, achieving enhanced force intensity and traveling range while maintaining a compact device geometry. These improvements highlight the potential of our design for advancing actuator performance in electrostatic systems.

Springs over-etch To probe the cause behind the augmented displacement readings, we conducted a meticulous geometric analysis using scanning electron microscopy (SEM). The images revealed that the springs within the device structures were over-etched, resulting in a 20% reduction in the width of thin single-beam springs compared to the original design. This deviation has significant implications, as it alters the overall stiffness of the device. Consequently, a new set of Multiphysics simulations was carried out to derive an adjusted stiffness function versus displacement curve for the actual fabricated geometry (Fig. 7). These revised simulations

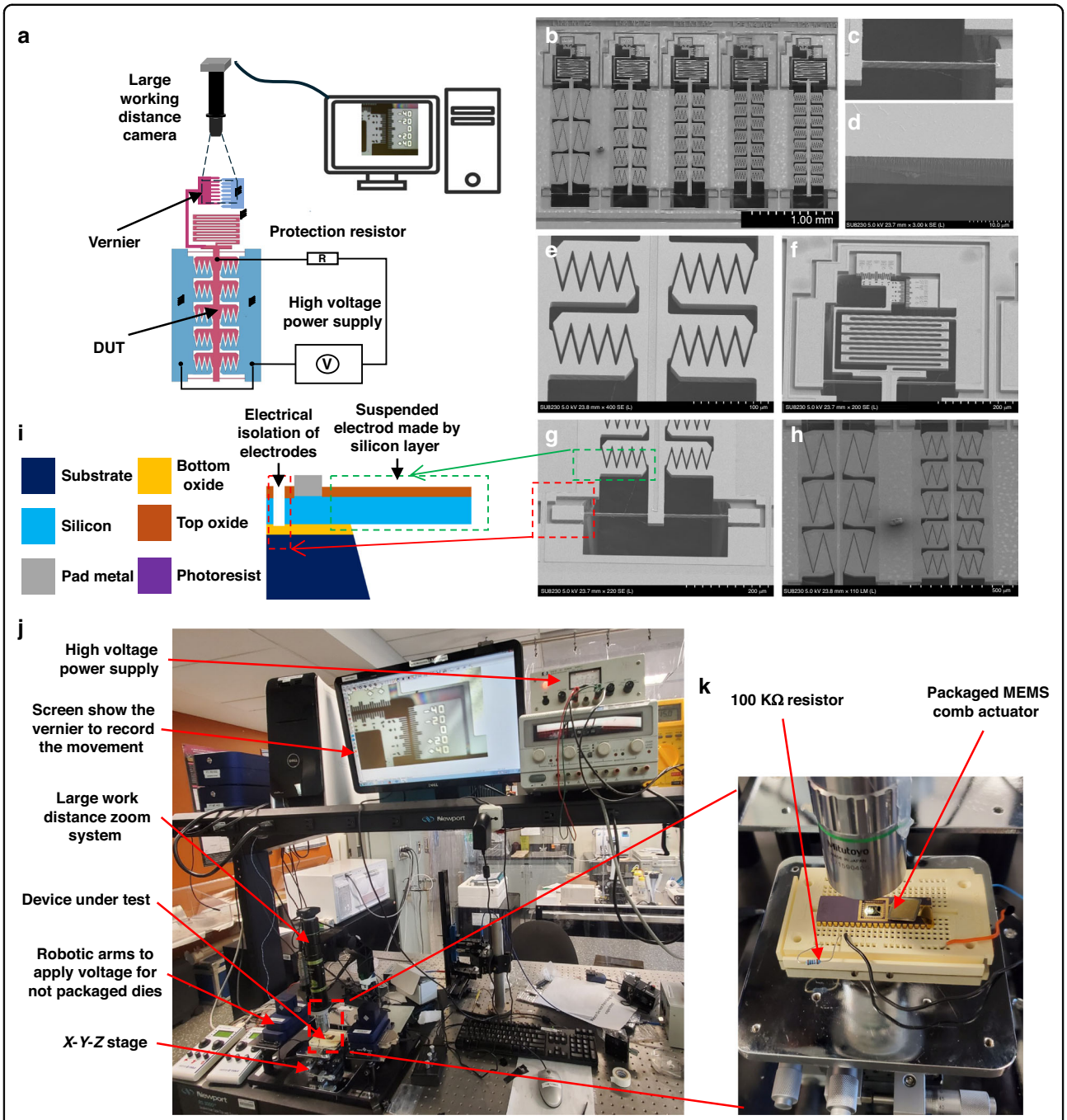

Fig. 5 Experimental Setup and SEM Characterization of MEMS Triangular Comb Drive Actuators. a Schematic showing the MEMS actuator setup with a DC bias, 100 kΩ protective resistor, and vernier system for displacement measurement. SEM images of MEMS comb actuators with varying finger configurations. **b** Top-down view showing finger diversity ($N_f = 1–5$). **c** 45° angled view detailing single beam springs. **d** 45° focused view of the suspended silicon layer. **e** Angled view of an actuator with 4 fingers. **f** Close-up of serpentine springs for electrical connectivity and vernier scale. **g** 45° view from below, revealing support structure. **h** Wider view of actuators with 1 and 2 fingers per arm. **i** Cross-sectional view of a suspended MEMS actuator structure and links the diagram to an SEM image, showing the suspended electrodes with precise electrical isolation. **j** Overall setup with high-voltage supply, protective resistor, and precision X-Y-Z stage for accurate positioning and probing. **k** Close-up view of packaged MEMS actuator with zoom system capturing real-time actuation

corroborated the experimental findings of increased displacement, attributing it to the reduced stiffness of the comb drives due to the over-etching.

Incorporating the updated stiffness function, we recalculated the force and force intensity for the fabricated devices, as illustrated in Fig. 6b, c. The results of these

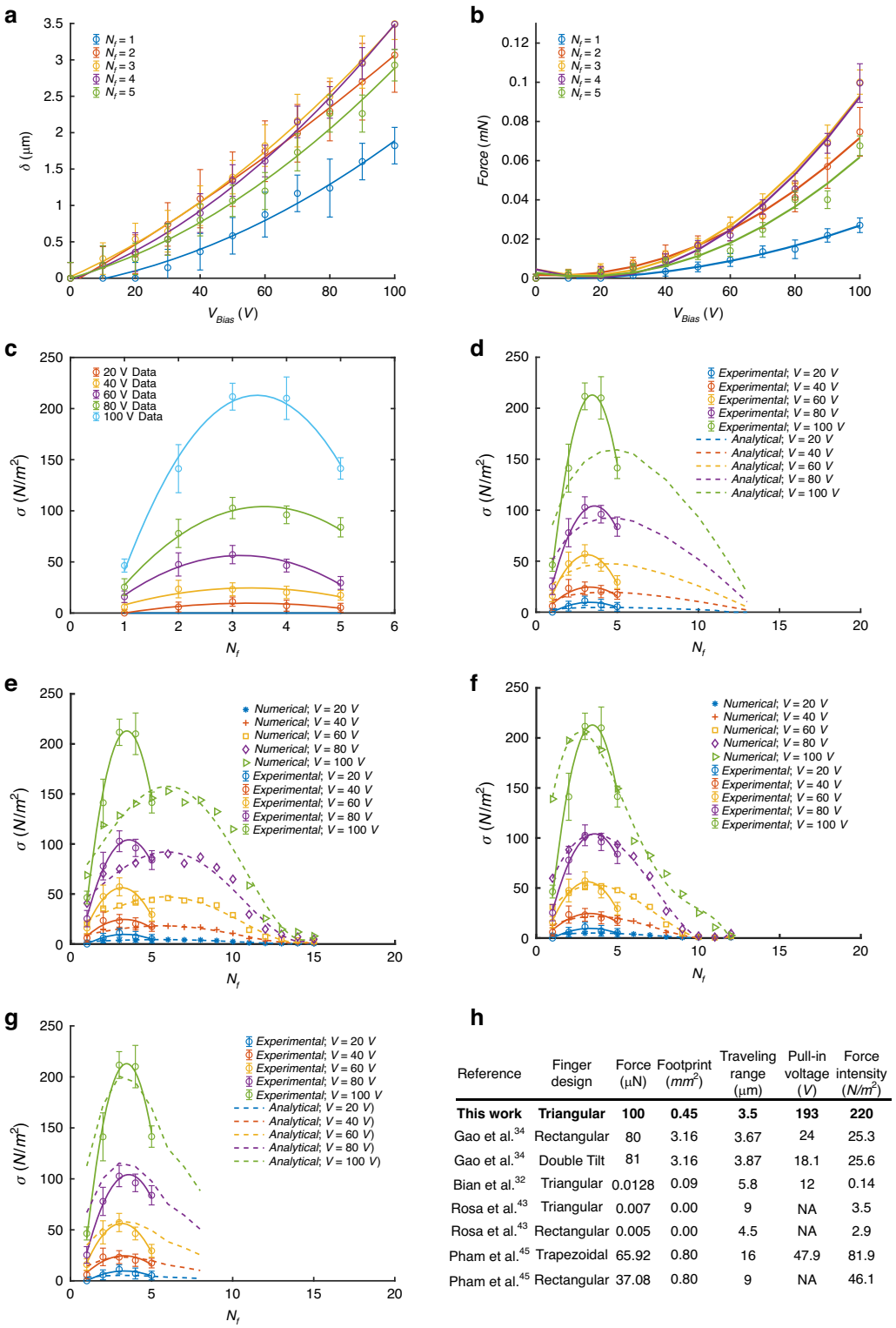

Reference	Finger design	Force (μN)	Footprint (mm^2)	Traveling range (μm)	Pull-in voltage (V)	Force intensity (N/m^2)
This work	**Triangular**	**100**	**0.45**	**3.5**	**193**	**220**
Gao et al.[34]	Rectangular	80	3.16	3.67	24	25.3
Gao et al.[34]	Double Tilt	81	3.16	3.87	18.1	25.6
Bian et al.[32]	Triangular	0.0128	0.09	5.8	12	0.14
Rosa et al.[43]	Triangular	0.007	0.00	9	NA	3.5
Rosa et al.[43]	Rectangular	0.005	0.00	4.5	NA	2.9
Pham et al.[45]	Trapezoidal	65.92	0.80	16	47.9	81.9
Pham et al.[45]	Rectangular	37.08	0.80	9	NA	46.1

Fig. 6 (See legend on next page.)

(see figure on previous page)
Fig. 6 Experimental Validation and Performance Comparison of Triangular Comb Drive Actuators. a–c Experimental results for MEMS comb drives with triangular fingers. **a** Displacement vs. voltage for devices with 1 to 5 fingers per arm, showing increased displacement compared to theory and simulation. **b** Force vs. Voltage, indicating higher force generation. **c** Force intensity vs. Number of Fingers per Arm (N_f), peaking at $N_f = 4$. Error bars denote measurement precision from three repeated tests. **d–f** Comparison of performance for various finger configurations and voltage levels before and after corrections to parameters a and d. **d** Discrepancies between original analytical simulations and experiments. **e** Similar comparison using numerical simulations. **f**, **g** Alignment of both analytical and numerical simulations with experimental outcomes after corrections, shifting peak force densities toward designs with fewer fingers per arm. **h** Comparison of key performance metrics (traveling range, electrostatic force, and footprint) for the proposed actuator design and prior configurations

recalculations reveal a slight elevation in the force and force intensity across the board, with a noticeable shift towards designs with fewer fingers (approximately $N_f = 4$) for the peak force intensity. Several factors may contribute to this observed increase in force and force intensity. The lower stiffness resulting from over-etching could allow for larger displacements for a given voltage before reaching the pull-in voltage, thereby as the stiffness function is not linear it might enhance the force exerted for a given voltage. Additionally, electrostatic effects could vary in actual devices due to small shape differences like edge effects or over-etching that the simulations might not capture.

Electrode over-etch To ensure our theoretical and experimental findings corresponded accurately with the actual performance of MEMS actuators, we conducted a thorough investigation into the impact of over-etching on actuator function. According to Eq. (1) the primary parameter influencing the force generated by the actuator, which is also associated with fabrication discrepancies, is the gap between electrodes (c). Equation (2) demonstrates that the electrode gap directly depends on the parameters d and α. Therefore, we will investigate how adjustments to these two parameters could align the simulation results with the actual fabrication outcomes.

To determine the necessary adjustments for the finger angle (α), we concentrated on (η), a key parameter that measures the electrode tips trim seen in scanning electron microscope (SEM) images. The electrode tips trim (η) parameter was found to increase with the number of fingers per actuator arm, likely due to the fill factor denoted as (ϕ) which represents the percentage of area that undergoes etching. To quantify this effect, we developed an equation based on experimental measurements and the calculation of the fill factor, as presented in Fig. 7f. The fill factor is determined by dividing the total etched area by the non-etched area of each device according to the design specifications. Consequently, η can be formulated as follows, capturing the tip trim for designs with different numbers of fingers:

$$\eta = \frac{6.5}{10^6}\phi + \eta_i \tag{21}$$

Here, η_i represents the etching observed in the design with one finger per arm which is 3 μm. Using η, we adjusted the initially designed angle, (α), to account for over-etching, resulting in a new effective angle, (α'), for each finger configuration. Figure 7b illustrates how we can calculate the α' based on the η, α and L_f :

$$\alpha' = \operatorname{atan}\left(\frac{\frac{L_f}{2}}{d_L - \eta}\right) \tag{22}$$

$$\alpha' = \operatorname{atan}\left(\frac{L_f}{L_f \cot\alpha - 2\eta}\right) \tag{23}$$

To calculate the (α') we presumed a straight-line etch path from the fingertip to the adjoining concave intersection as depicted by the dashed black lines in Fig. 7c. The true etch profile deviates from this assumption; red lines indicate where the angle has broadened due to over-etching up to a length (s) shown in Fig. 7e, while the green lines denote areas where the original angle is maintained.

This led to the introduction of the over-etch impact factor (τ), which corrects for the new α:

$$\tau = \frac{2(s+\eta)}{b} \tag{24}$$

where b is given by Eq. (3) and measurement from the fabricated devices shows that $s = 12\,\mu m$. Beyond five fingers per arm, this overetch impact factor settles at 1, signifying that the over-etching effect levels off, as corroborated by Fig. 7d for finger counts of six or greater. Thus, adding more fingers doesn't significantly alter the over-etching profile, however the α_1 still increasing due to the η and ϕ.

Therefor the final relation for η to calculate the corrected angle (α_1) based on Eq. (23) would be as follows:

$$\eta_{(N_f<6)} = \tau\left(\frac{6.5}{10^6}\phi + \eta_i\right) \tag{25}$$

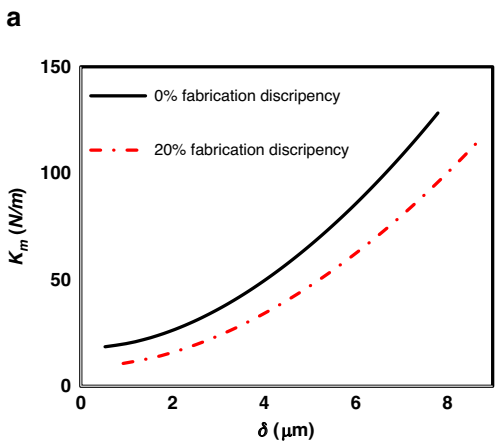

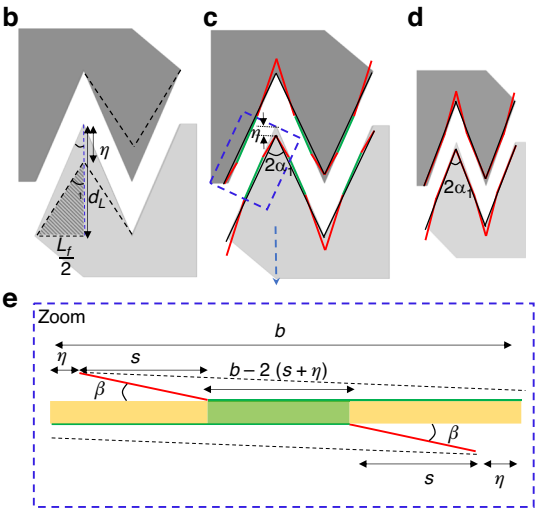

f

N_f (Number of fingers)	η (μm) (Tip trim, experimental)	η (μm) (Finger tip trim)	ϕ (1) (Fill factor)	τ (1) (Over etch impact)	α' (°) (Effective angel)	d' (μm) (Effective d)
1	3.30	3.62	0.10	0.11	10.21	19.19
2	3.90	4.04	0.16	0.24	10.26	19.48
3	4.20	4.35	0.21	0.39	10.35	19.84
4	4.30	4.59	0.24	0.57	10.52	20.30
5	4.50	4.77	0.27	0.78	10.79	20.85
6	-	4.91	0.29	1.00	11.17	21.46
7	-	5.02	0.31	1.00	11.39	21.51
8	-	5.12	0.33	1.00	11.61	21.56

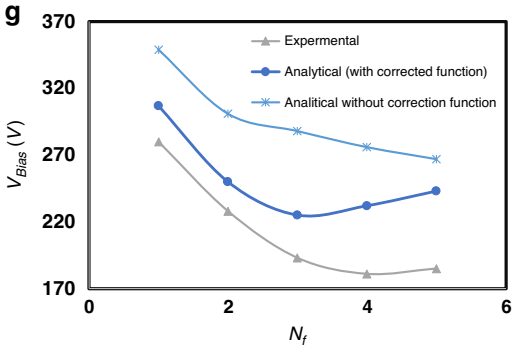

h

Number of fingers	Maximum force (*mN*)	Maximum traveling range (μm)	Maximum bias voltage (V)
1	2.7	11.2	350
2	2.5	11	300
3	2.45	10.9	289
4	2.4	10.7	276
5	2.25	10.5	266

Fig. 7 Impact of Fabrication Tolerances and Over-Etching on Triangular Comb Drive Performance. a Singel beam spring over-etch study. The graph shows Stiffness vs. Displacement curves comparing ideal design (solid black) and a device with 20% reduced spring width (dashed red), showing decreased stiffness and increased displacement due to fabrication tolerances. Analysis of over-etching effects on MEMS actuator electrodes. **b** sketch for calculation of the effective angle (a_1) post-overetch using tip over-etch (η), initial angle (a), and finger length (L_f). **c** Comparison of designed (black dash line) vs. actual (red over etched parts and green non over etched parts) electrode profiles after over-etching. **d** Analysis for configurations with 6+ fingers shows stabilized over-etch effects. **e** Expanded view differentiates over-etched (orange) and unchanged (green) regions, highlighting changes in electrode angle (a') and gap. **f** Detailed adjustments and measurements for MEMS actuators with varying numbers of fingers per arm. **g** Pull-in voltage for different comb drive configurations ($N = 1$ to $N = 5$) using the analytical model, corrected model, and experimental results. **h** Maximum force, travel range, and bias voltage for each configuration based on the analytical calculations without correction function, highlighting performance differences across designs

$$\eta_{(N_f \geq 6)} = \frac{6.5}{10^6}\phi + \eta_i \tag{26}$$

We have now detailed the adjustments necessary for the finger angle. The final parameter requiring correction to align simulation results with experimental findings is the gap (d). Based on experimental outcomes, after correcting the angle, the following adjustment to (d) ensures a close match between the simulated results and those observed in fabricated devices.

$$d' = d + \frac{\eta}{2} - 1 \tag{27}$$

Here, d' is the corrected gap for each design and varies based on η. This adjustment reflects our observation that, although theoretical predictions suggest the gap d should increase by an amount equal to the electrode tip trim (η), actual experimental results necessitate modifying this increase by applying a coefficient and constant value to η in our case. This modification is due to the fact that the actual etch profile significantly diverges from the simple straight-line model initially proposed in Fig. 7. The precise adjustment of d using this coefficient was crucial for aligning the theoretical model with observed results, similar to how we introduced the over-etch impact factor for correcting the angle (α).

As shown in Fig. 7f, we present a comprehensive overview of the corrections applied across different designs of MEMS actuators. This table encapsulates critical parameters including the number of fingers per arm, the experimentally measured and calculated tip trims, fill factors, over-etch impact factors, corrected effective angles, and effective finger tip-to-tip separation. The data clearly demonstrates how adjustments based on empirical observations and calculated corrections effectively reconcile theoretical predictions with real-world experimental outcomes. The table serves as a crucial reference for understanding the impact of fabrication discrepancies on the performance of MEMS actuators and the effectiveness of our correction methodology.

Validation of correction functions To ensure that our theoretical predictions accurately reflect the actual performance of MEMS comb drives, we undertook a comprehensive restimulation of the devices incorporating the newly defined correction functions for the finger angle (α) and the electrode gap (d). These functions were integrated into both analytical and numerical models to refine our simulations based on post-fabrication insights.

Figure 6 illustrates the results of these refined simulations, compared across different voltage levels and numbers of fingers. Panels (d) and (e) display the original simulation outcomes compared with experimental data before applying the corrections, highlighting the initial discrepancies. Subsequently, panels (f) and (g) demonstrate the alignment of both analytical and numerical simulations with the experimental results after the correction functions were applied. This process was critical in validating the effectiveness of the corrections, as it not only confirmed their accuracy but also fine-tuned the parameters to achieve a more precise match between the simulated outcomes and the actual fabrication data.

The refined simulations show a notable correction in the peak force densities, which shifted towards designs with fewer fingers per arm. This adjustment indicates a significant improvement in the model's ability to predict physical device behavior under various operational conditions. By enhancing the predictive accuracy of our simulations, we establish a more reliable framework for the design and optimization of future MEMS devices. This methodical approach ensures that theoretical models can be confidently used to predict real-world performance, providing a solid foundation for the continued development and refinement of MEMS technologies.

Discussion

This study introduces a sophisticated approach to the design of electrostatic comb drives, particularly focusing on triangular finger geometry to enhance performance metrics critical for silicon photonic MEMS actuators. Our research has shown that triangular finger configurations, due to their geometric specificity, significantly augment both force intensity and traveling range. This significant enhancement in performance metrics, due to the unique triangular geometry, is an aspect that previous studies in the field have not extensively addressed[11,31–34,43,48–51]. These are key parameters for high-speed, high-force applications in photonic integrated circuits, where maintaining high force output and extensive traveling range within a compact area is essential[4,7–24,30].

Our exploration into the optimization of comb finger angles and dimensions within a constrained spatial footprint reveals that this angled approach significantly reduces the actuator's footprint without compromising on traveling range and force output. This finding addresses a critical challenge in MEMS design, especially important in densely packed optical networks or integrated photonic systems where space efficiency is crucial.

Moreover, our study delves into how the configuration of fingers within the comb structure can impact overall performance a factor seldom considered in previous works. By experimenting with different configurations of finger arrangements, we have identified optimal patterns that enhance the comb drive's operational efficiency, highlighting the importance of detailed microstructural design in MEMS actuators.

A significant advancement introduced in this study is the development of correction functions to compensate for fabrication discrepancies such as over-etching. By incorporating these functions during the design phase, we ensure that the final device performance closely adheres to the intended specifications. This strategy not only enhances device reliability but also streamlines the transition from prototype to production by mitigating common fabrication issues that can lead to device failure or suboptimal performance.

Despite these advancements, there remain limitations that pave the way for future research. Our modeling assumptions, although robust, may not capture all real-world operational conditions such as temperature and mechanical stresses, suggesting that our findings, while promising, may behave differently under varied environmental conditions. Additionally, while our study has significantly advanced the correction functions for fabrication discrepancies, further refinement is possible. By iterating the design and fabrication process, we aim to enhance these correction functions continuously, improving their ability to compensate for manufacturing variations proactively.

Implementing chamfering at the fingertip could help reduce tip loss and improve shape retention during fabrication. However, this alone may not fully mitigate over-etching issues, as over-etching also occurs due to the reduced silicon density at the fingertip caused by the proximity to adjacent gaps. We prioritized maintaining maximum electrode overlap to achieve higher force intensity, which would be slightly compromised by chamfering the tip. As a future consideration, chamfering at the tip may be explored to enhance fabrication repeatability and reliability, though this may come at the cost of a marginal decrease in force intensity.

In future works, we will focus on implementing these improved correction functions and on testing the scalability of our designs by integrating these actuators into larger-scale photonic systems to evaluate their performance in real-world conditions. This will help in assessing the practical application of our designs in operational environments and may lead to new insights into the adaptability of our methods across different platforms and applications.

Our ongoing efforts will also involve targeted improvements in the fabrication process itself, such as refining etching techniques and enhancing in-process monitoring to ensure greater adherence to design specifications. These improvements aim to bridge the gap between theoretical models and actual device performance, thereby increasing the fidelity and reliability of MEMS devices.

By concentrating on these areas, we aim to advance the field of MEMS actuators, particularly for silicon photonics, where precision and efficiency are paramount. The iterative refinement of design and fabrication methods is expected to enhance the predictability and reliability of MEMS devices, thereby supporting their integration into more complex systems and applications.

Materials and methods

Fabrication

In this study, the fabrication of electrostatic comb actuators was accomplished using the PiezoMUMPs process[46] at the MEMSCAP foundry, a variation of the standard MUMPs process designed specifically for devices using SOI substrates. The process began with an SOI wafer, comprising layers of silicon (10 μm), oxide (1 μm), and substrate (400 μm).

The procedure involved doping and annealing the silicon layer, followed by phosphosilicate glass layer removal via wet chemical etching. The silicon was then patterned and etched to the oxide layer for various mechanical and electrical structures. A 2000 Angstroms thermal oxide layer was grown for insulation, patterned, and etched using a reactive ion etch (RIE).

Although the process typically includes an Aluminum Nitride piezoelectric layer, this step was not utilized in our fabrication. A PadMetal layer composed of chrome (20 nm) and aluminum (1 μm) was deposited, allowing for fine metal features. This layer was patterned using a liftoff process but was restricted to areas not etched in the silicon device layer due to the subsequent Deep RIE steps.

Deep RIE was used to pattern the silicon precisely. Following this, the wafer was inverted for bottom-side patterning and etching, which defined the Substrate layer. The final steps included removing the Buried Oxide layer in designated regions, releasing mechanical structures through a dry etch process, and dicing the wafers with a laser.

The SOI substrate's use was vital for enhancing mechanical stability and reducing parasitic capacitance, important for high-performance and high-speed active photonic devices that demand high force, broad traveling range, and reliable, high-speed MEMS actuators[52–54].

Figure 5i shows the cross-section of the suspended structure and demonstrates how suspended, electrically isolated electrodes connected via a single beam spring, essential for dynamic actuation and structural integrity. The corresponding SEM image validates the precision of our SOI-MEMS fabrication, aligning the theoretical design with the manufactured device.

Experimental setup

For the execution of our experiments, we meticulously packaged the fabricated MEMS dies, ensuring all pads were accessible for photonics wire bonding. The dies were enclosed in the Spectrum Semiconductor Materials, Inc. SSM P/N CSB40457 ceramic package, which provided a cavity size of 8.64 mm by 8.64 mm with 40 pins, perfectly accommodating our requirements for secure and reliable electrical connections.

The voltage application was carefully managed with a DC high-voltage supply. To safeguard our devices during testing, we incorporated a 100 kΩ resistor in the circuit, acting as a protective measure against any potential pull-in events that could damage the delicate MEMS structures.

The FemtoTools FT-MTA02 Micromechanical Testing and Assembly Station was the cornerstone of our experimental setup, utilized for its precision handling and imaging capabilities. The FT-MTA02 original imaging system has a 3-megapixel CMOS USB camera and an adjustable zoom system, providing a field of view ranging from 15 mm × 11 mm down to 2.2 mm × 1.7 mm and an optical resolution of 3 µm. However, for our measurements, we need to have submicron precision to precisely measure the actuator movement. Therefore, the original imaging system of this device was augmented by replacing the objective lens with a 20× objective lens, significantly enhancing our ability to detect minute displacements down to 0.2 µm. In conjunction with the vernier scale design, this setup allowed us to precisely measure movements with an accuracy of 0.25 µm through image processing techniques.

The FemtoTools robotic arm and the micropositioner, integral components of the FT-MTA02 system, were employed to test unpackaged dies with exceptional accuracy. A 20 µm needle was used to probe the pads of our devices, facilitating exact voltage application for the unpackaged dies.

Each device was rigorously tested in triplicate to ensure consistency and reliability, informing the error bars presented in our graphs. The electrostatic force at different voltage levels was calculated from the measured displacement data, utilizing the known stiffness of the comb drives, which was critical for evaluating the actuator's performance. The force intensity for each prototype was calculated using the calculated force and the measured footprint area of the comb drive, which is essential for assessing the efficiency of the actuator designs. The combination of the precise FemtoTools FT-MTA02 system, along with the robust packaging solution provided by Spectrum Semiconductor Materials, enabled a highly controlled and accurate investigation into the performance characteristics of the MEMS comb actuators, crucial for advancing the field of silicon photonics.

To illustrate the experimental arrangement, Fig. 5a and j, k displays the setup, including the high voltage power supply, screen for displaying the vernier readings, zoom system, packaged MEMS comb actuator, and the X-Y-Z stage.

Conclusion and future works

Conclusion

In this study, we conducted a detailed parametric analysis of electrostatic comb drives, focusing specifically on angled finger configurations for use in active silicon photonic devices. Our analysis explored multiple design parameters, such as the count of fingers per arm, their dimensions, width, angle, and arm dimensions. We pinpointed configurations that optimize force intensity, travel range, and reliability for high-speed MEMS actuators. The experimental results demonstrate that these optimized configurations significantly outperform traditional designs in terms of displacement and force intensity at given voltage levels, highlighting the effectiveness of triangular finger comb drives in meeting the stringent demands of advanced MEMS actuators.

We also identified critical influences of manufacturing precision on device performance, with particular emphasis on how over-etching can significantly alter actuator behavior. This underscores the importance of precise manufacturing and stringent process control. Additionally, our findings contribute to a better understanding of the physical behavior of MEMS devices under real-world conditions, laying a solid foundation for further research and development.

Particularly, our study addresses the complex challenge within silicon photonics applications that require actuators with a compact footprint, high force, and wide traveling range. We successfully optimized triangular finger comb drives to simultaneously meet these conflicting parameters, advancing the design and reliability of MEMS actuators for high-performance optical devices. These enhancements in design methodology and fabrication processes are crucial for evolving the capabilities of MEMS actuators to meet the needs of high-speed, high-precision applications across various technological sectors.

Acknowledgements
The authors acknowledge the support of NSERC Discovery, NSERC RTI, NSERC Strategic, and Concordia Research Chair grants of Packirisamy. Additionally, we acknowledge the design software support and fabrication services from CMC Microsystems.

Author contributions
M.F. and M.P. conceived the study. M.F. conducted the detailed simulations, generated the layout for fabrication, performed experimental validations, analyzed the results, and drafted the manuscript. M.P. supervised the project, provided critical revisions to the manuscript, and guided the overall research direction. Both authors reviewed the manuscript.

Competing interests
The authors declare no competing interests.

Supplementary information The online version contains supplementary material available at https://doi.org/10.1038/s41378-025-00906-6.

Received: 1 June 2024 Revised: 6 December 2024 Accepted: 26 January 2025
Published online: 24 October 2025

References
1. Zhao, X., Duan, G., Li, A., Chen, C. & Zhang, X. Integrating microsystems with metamaterials towards meta devices. *Microsyst. Nanoeng.* **5**, 1–17 (2019).

2. Zheyi, H., Colburn, S., Majumdar, A. & Böhringer, K. F. MEMS-actuated meta surface Alvarez lens. *Microsyst Nanoeng* **6**, 79 (2020).
3. Bifano, T. MEMS deformable mirrors. *Nat. Photon* **5**, 21–23 (2011).
4. Wu, M. C., Solgaard, O. & Ford, J. E. Optical MEMS for lightwave communication. *J. Lightwave Technol.* **24**, 4433–4454 (2006).
5. Quack, N. et al. MEMS-enabled silicon photonic integrated devices and circuits. *IEEE J. Quantum Electron.* **56**, 1–10 (2019).
6. Quack, N. et al. Integrated silicon photonic MEMS. *Microsyst. Nanoeng.* **9**, 1–22 (2023).
7. Sharma, S., Kohli, N., Brière, J., Ménard, M. & Nabki, F. Translational MEMS platform for planar optical switching fabrics. *Micromachines* **10**, 435 (2019).
8. Bulgan, E., Kanamori, Y. & Hane, K. Submicron silicon waveguide optical switch driven by microelectromechanical actuator. *Appl. Phys. Lett.* **92**, 101110 (2008).
9. Fasihanifard, M. & Packirisamy, M. Methods and systems of mechanical tuning multi-channel optical components. U.S. Patent Application No. 18/325,268. (2023).
10. Chollet, F. Devices based on co-integrated MEMS actuators and optical waveguide: a review. *Micromachines* **7**, 18 (2016).
11. Errando-Herranz, C. et al. MEMS for photonic integrated circuits. *IEEE J. Sel. Top. Quantum Electron.* **26**, 1–16 (2020).
12. Stepanovsky, M. A comparative review of MEMS-based-optical cross-connects for all-optical networks from the past to the present day. *IEEE Commun. Surv. Tutor.* (2019).
13. Bogaerts, W. et al. MORPHIC: programmable photonic circuits enabled by silicon photonic MEMS. In *Silicon Photonics XV* vol. 11285 1128503 (International Society for Optics and Photonics, 2020).
14. Zhou, G., Lim, Z. H., Qi, Y., Chau, F. S. & Zhou, G. MEMS gratings and their applications. *Int. J. Optomechatronics* **15**, 61–86 (2021).
15. Grade, J. D., Yasumura, K. Y. & Jerman, H. Advanced, vibration-resistant, comb-drive actuators for use in a tunable laser source. *Sens. Actuators A Phys.* **114**, 413–422 (2004).
16. Ahdab, R., el, Sharma, S., Nabki, F. & Ménard, M. Wide-band silicon photonic MOEMS spectrometer requiring a single photodetector. *Opt. Express* **28**, 31345–31359 (2020).
17. Omran, H. et al. Deeply-etched optical MEMS tunable filter for swept laser source applications. *IEEE Photonics Technol. Lett.* **26**, 37–39 (2014).
18. Brière, J., Beaulieu, P.-O., Saidani, M., Nabki, F. & Menard, M. Rotational MEMS mirror with latching arm for silicon photonics. In *MOEMS and Miniaturized Systems XIV* vol. 9375 937507 (International Society for Optics and Photonics, 2015).
19. Akihama, Y. & Hane, K. Single and multiple optical switches that use free-standing silicon nanowire waveguide couplers. *Light Sci. Appl.* **1**, e16–e16 (2012).
20. Errando-Herranz, C., Thomas, N. L. & Gylfason, K. B. Low-power optical beam steering by microelectromechanical waveguide gratings. *Opt. Lett.* **44**, 855–858 (2019).
21. Fasihanifard, M. & Packirisamy, M. Mechanically actuated asymmetric slab waveguide: optical and mechanical design considerations. In *Proc. Photonics North (PN)* 1–1 https://doi.org/10.1109/PN56061.2022.9908387 (2022).
22. Fasihanifard, M., Pottier, P. & Packirisamy, M. MEMS Enabled asymmetric slab waveguide for continuously tunable filter. In *Proc. Photonics North (PN)* 1–1 https://doi.org/10.1109/PN52152.2021.9597909 (2021).
23. Park, Y. & Choi, S. H. Miniaturization of optical spectroscopes into Fresnel microspectrometers. *J. Nanophotonics* **7**, 077599 (2013).
24. Packirisamy, M. & Pottier, P. Wavelength tunable optical sources, filters and detectors (2018).
25. Bell, D. J., Lu, T. J., Fleck, N. A. & Spearing, S. M. MEMS actuators and sensors: observations on their performance and selection for purpose. *J. Micromech. Microeng.* **15**, S153 (2005).
26. Zhou, G. & Lee, C. *Optical MEMS, Nanophotonics, and Their Applications* (CRC Press, 2017).
27. Zhang, W.-M., Yan, H., Peng, Z.-K. & Meng, G. Electrostatic pull-in instability in MEMS/NEMS: a review. *Sens. Actuators A Phys.* **214**, 187–218 (2014).
28. Chai, J. et al. Review of MEMS-based Fourier transform spectrometers. *Micromachines* **11**, 214 (2020).
29. Wang, C. et al. Design of a large-range rotary microgripper with freeform geometries using a genetic algorithm. *Microsyst. Nanoeng.* **8**, 1–14 (2022).
30. Fasihanifard, M., Pottier, P. & Packirisamy, M. Design of an Integrated Multi-Band Continuous Optical Filter using Mechanical Tuning. In *Proc. Photonics North (PN)* 1–1 https://doi.org/10.1109/PN58661.2023.10222990 (2023).
31. Hoffmann, D., Folkmer, B. & Manoli, Y. Analysis and characterization of triangular electrode structures for electrostatic energy harvesting. *J. Micromech. Microeng.* **21**, 104002 (2011).
32. Bian, W., Zhao, J. & You, Z. Low voltage, high speed and small area in-plane MEMS switch. *J. Micromech. Microeng.* **29**, 065014 (2019).
33. Zhao, J. & Gao, Y. Electrostatic comb-drived actuator for MEMS relay/switch. in *Micro Electro Mechanical Systems* (ed. Huang, Q.-A.) 907–927. https://doi.org/10.1007/978-981-10-5945-2_30 (Springer, 2018).
34. Gao, Y., You, Z. & Zhao, J. Electrostatic comb-drive actuator for MEMS relays/switches with double-tilt comb fingers and tilted parallelogram beams. *J. Micromech. Microeng.* **25**, 045003 (2015).
35. Ye, W. & Mukherjee, S. Design and fabrication of an electrostatic variable gap comb drive in micro-electro-mechanical systems. *Comput. Model. Eng. Sci.* **1**, 111–120 (2000).
36. Engelen, J. B. C., Lantz, M. A., Rothuizen, H. E., Abelmann, L. & Elwenspoek, M. C. Improved performance of large stroke comb-drive actuators by using a stepped finger shape. In *Proc. TRANSDUCERS 2009–2009 International Solid-State Sensors, Actuators and Microsystems Conference,* 1762–1765 (IEEE, 2009).
37. Veroli, A. et al. An approach to the extreme miniaturization of rotary comb drives. *Actuators* **7**, 70 (2018).
38. Eltagoury, Y. M., Soliman, M., Sabry, Y. M., Alotaibi, M. J. & Khalil, D. Electrostatic comb-drive actuator with high in-plane translational velocity. *Micromachines* **7**, 188 (2016).
39. Li, R. et al. Design, modelling and characterization of comb drive MEMS gap-changeable differential capacitive accelerometer. *Measurement* **169**, 108377 (2021).
40. Shakoor, R. I., Chughtai, I. R., Bazaz, S. A., Hyder, M. J., & Masood-ul-Hassan. Numerical simulations of MEMS comb-drive using coupled mechanical and electrostatic analyses. In *Proc. International Conference on Microelectronics* 344–349 https://doi.org/10.1109/ICM.2005.1590098 (2005).
41. Fasihanifard, M., Pottier, P. & Packirisamy, M. Asymmetric stiff slab waveguide actuation with footprint-optimized mechanical platform. In *Proc. Photonics North (PN)* 1–1 https://doi.org/10.1109/PN50013.2020.9166952 (2020).
42. Lu, Y., Marty, F., Galayko, D., Laheurte, J.-M. & Basset, P. A power supply module for autonomous portable electronics: ultralow-frequency MEMS electrostatic kinetic energy harvester with a comb structure reducing air damping. *Microsyst. Nanoeng.* **4**, 1–13 (2018).
43. Rosa, M. A., Dimitrijev, S. & Harrison, H. B. Improved operation of micromechanical comb-drive actuators through the use of a new angled comb finger design. *J. Intell. Mater. Syst. Struct.* **9**, 283–290 (1998).
44. Ye, W., Mukherjee, S. & MacDonald, N. C. Optimal shape design of an electrostatic comb drive in microelectromechanical systems. *J. Microelectromech. Syst.* **7**, 16–26 (1998).
45. Pham, P. H., Hoang, K. T. & Nguyen, D. Q. Trapezoidal-shaped electrostatic comb-drive actuator with large displacement and high driving force density. *Microsyst. Technol.* **25**, 3111–3118 (2019).
46. Piezo standard technology. https://science.xyz/docs/d/mems-piezo/index.
47. Palmer, H. B. The capacitance of a parallel-plate capacitor by the Schwartz-Christoffel transformation. *Electr. Eng.* **56**, 363–368 (1937).
48. Bian, W., Zhao, J., You, Z. & Sun, X. A restoring force boosting structure with flexible stiction recovery electrode for MEMS relays/switches. In *Proc. 32nd International Conference on Micro Electro Mechanical Systems (MEMS)* 986–989 https://doi.org/10.1109/MEMSYS.2019.8870656 (IEEE, 2019).
49. Kang, S., Kim, H. C. & Chun, K. A low-loss, single-pole, four-throw RF MEMS switch driven by a double-stop comb drive. *J. Micromech. Microeng.* **19**, 035011 (2009).
50. Weis, T. A. S., Lahijani, B. V., Tsoukalas, K., Albrechtsen, M. & Stobbe, S. Design, fabrication, and characterization of electrostatic comb-drive actuators for nanoelectromechanical silicon photonics. Preprint at https://doi.org/10.48550/arXiv.2307.01122 (2023).
51. Sharma, S. et al. Integrated 1×3 MEMS silicon nitride photonics switch. *Opt. Express* **30**, 22200–22220 (2022).
52. Paul, S. *Surface Micromachined Widely Tunable VCSEL and OAM-Filter for Optical Data Transmission* (Technische Universität, 2019).
53. Oxaal, J., Foster, D., Hella, M. & Borca-Tasciuc, D.-A. Investigation of gap-closing interdigitated capacitors for electrostatic vibration energy harvesting. *J. Micromech. Microeng.* **25**, 105010 (2015).
54. Khan, F. & Younis, M. I. RF MEMS electrostatically actuated tunable capacitors and their applications: a review. *J. Micromech. Microeng.* **32**, 013002 (2021).